



**HAL**  
open science

# When zircon drowns: Elusive geochronological record of water-fluxed orthogneiss melting in the Velay dome (Massif Central, France)

Simon Couzinié, Pierre Bouilhol, Oscar Laurent, Linda Marko, Jean-François Moyen

## ► To cite this version:

Simon Couzinié, Pierre Bouilhol, Oscar Laurent, Linda Marko, Jean-François Moyen. When zircon drowns: Elusive geochronological record of water-fluxed orthogneiss melting in the Velay dome (Massif Central, France). *Lithos*, 2021, 384-385, pp.105938. 10.1016/j.lithos.2020.105938 . hal-03231939

**HAL Id: hal-03231939**

**<https://hal.science/hal-03231939>**

Submitted on 18 Nov 2021

**HAL** is a multi-disciplinary open access archive for the deposit and dissemination of scientific research documents, whether they are published or not. The documents may come from teaching and research institutions in France or abroad, or from public or private research centers.

L'archive ouverte pluridisciplinaire **HAL**, est destinée au dépôt et à la diffusion de documents scientifiques de niveau recherche, publiés ou non, émanant des établissements d'enseignement et de recherche français ou étrangers, des laboratoires publics ou privés.

1 **When zircon drowns: elusive geochronological record of water-fluxed**  
2 **orthogneiss melting in the Velay dome (Massif Central, France)**

3 Simon Couzinié<sup>a,b</sup>, Pierre Bouilhol<sup>a</sup>, Oscar Laurent<sup>c,d</sup>, Linda Marko<sup>e</sup>, Jean-François  
4 Moyen<sup>b</sup>

5 <sup>a</sup> Université de Lorraine, CNRS, CRPG, F-54000 Nancy, France

6 <sup>b</sup> Université de Lyon, Université Jean Monnet, CNRS–IRD, Laboratoire Magmas & Volcans, F-  
7 42023 Saint Etienne, France

8 <sup>c</sup>ETH Zürich, Department Erdwissenschaften, Institute for Geochemistry and Petrology,  
9 Clausiusstrasse 25, CH-8092 Zürich, Switzerland

10 <sup>d</sup>CNRS, Observatoire Midi-Pyrénées, Géosciences Environnement Toulouse, 14 avenue E.  
11 Belin, F-31400 Toulouse, France

12 <sup>e</sup>Goethe Universität Frankfurt, Institut für Geowissenschaften, Altenhöferallee 1, D-60438  
13 Frankfurt am Main, Germany

14

15 **Keywords:** zircon U–Pb geochronology, water-fluxed melting, anatexis, Variscan  
16 orogeny, Velay dome

17

18

19

20

21

22

23

24

25  
26  
27  
28  
29  
30  
31  
32  
33  
34  
35  
36  
37  
38  
39  
40  
41  
42  
43  
44  
45  
46  
47  
48  
49  
50  
51  
52  
53  
54  
55

## Abstract

Zircon U–Pb geochronology is routinely performed to unravel the timing and duration of melting events within the continental crust. A comprehensive understanding of the zircon behavior during anatexis is therefore paramount to accurately assess the impact of crustal melting on orogenic processes. We report on an anatectic system from the southern part of the Velay dome (Variscan French Massif Central) encompassing late Carboniferous migmatites developed at the expense of peraluminous orthogneisses and associated with (leuco)granite bodies intrusive at higher structural levels. Our zircon U-Pb geochronological survey (494 analyzed grains) evidences a very scant record of the Variscan anatectic event. Indeed, oscillatory-zoned melt-precipitated zircon grains extracted from metatexites, leucosomes and (leuco)granites almost systematically yielded the late Neoproterozoic crystallization age of the felsic igneous protolith. Field and petrographic observations, whole-rock geochemical signatures, phase equilibrium and thermodynamically-constrained trace element modelling collectively indicate that partial melting of the orthogneisses took place at  $T \sim 700^\circ\text{C}$  and was fluxed by ingress of external water. The lack of new zircon growth is ascribed to a range of processes ultimately related to the low melting temperature including limited zircon solubility in the melt phase, occlusion of zircon in non-reacting source biotite and sluggish zircon dissolution kinetics. Peraluminous orthogneisses, yet highly fusible due to their “eutectic” subsolidus mineral assemblage, exhibit a very limited zircon record of low temperature water-fluxed melting. Thus, zircon has little potential to provide reliable chronological constraints on water-fluxed melting episodes affecting such lithologies.

## 1. Introduction

57 Crustal melting has a profound impact on the mechanical and rheological behavior of  
58 the continental crust (Rey et al., 2009; Rosenberg and Handy, 2005; Vanderhaeghe  
59 and Teyssier, 2001). Deciphering orogenic processes thus requires an assessment of  
60 the timing and duration of anatexis events. For that purpose, zircon, an accessory  
61 mineral commonly crystallizing in intermediate to felsic magmas, has proven a very  
62 efficient tool as it can be accurately and precisely dated using the U–Pb method.  
63 Accordingly, many studies concluded that anatexis melt can be present for long  
64 periods of time within the crust based on the zircon U–Pb age distribution of migmatites  
65 or anatexis granites (Guergouz et al., 2018; Harley, 2016; Korhonen et al., 2013;  
66 Laurent et al., 2018; Laurent et al., 2017; Lemirre et al., 2019; O'Brien and Miller, 2014;  
67 Rubatto et al., 2013; Rubatto et al., 2009; Taylor et al., 2019).

68 Low temperature ( $T < 750^{\circ}\text{C}$ ) anatexis generates significant melt fractions and greatly  
69 impacts crustal rheology only if melting is fluxed by the addition of external water, a  
70 more common process than generally thought (see Weinberg and Hasalová (2015)  
71 and references therein). The zircon record of low temperature water-fluxed melting  
72 remains unclear, as studies conducted on anatexis systems having experienced such  
73 melting conditions are scarce and yielded contrasting results. Rubatto et al. (2009)  
74 report extensive new zircon crystallization in migmatites, allowing an accurate  
75 assessment of the timing of partial melting. In contrast, other authors (e.g. Brouand et  
76 al. (1990), Oliver et al. (1999)) document cases of migmatites nearly lacking any new  
77 zircon growth related to the anatexis event, but without a clear assessment of the role  
78 of water-fluxed melting.

79 We address this issue based on a case study from the Velay dome (French Massif  
80 Central), an archetypal granite–migmatite dome formed at the end of the late Paleozoic  
81 Variscan orogeny, which has been a foundation stone for many concepts regarding  
82 the role of partial melting in orogen dynamics (Burg and Vanderhaeghe, 1993; Costa  
83 and Rey, 1995; Ledru et al., 2001; Vanderhaeghe et al., 2020; Vanderhaeghe and  
84 Teyssier, 2001). Recently, it has been proposed that the supply of heat and  $\text{H}_2\text{O}$  from  
85 granitic magmas emplaced at mid-crustal levels played an important role in the  
86 development of the Velay dome migmatites (Barbey et al., 2015; Villaros et al., 2018),  
87 making them an ideal target for this study. We document the field relationships,

88 petrography, whole-rock geochemistry and zircon U–Pb systematics of migmatites and  
89 associated anatectic (leuco)granites from the Masméjean antiform which is located at  
90 the southwesternmost part of the Velay dome (Fig. 1). We unravel their petrogenesis  
91 and discuss the scant zircon record of crustal melting as observed from our dataset.  
92 Our results highlight the limitations of zircon in deciphering the duration of water-fluxed  
93 crustal melting events and bear implications on the zircon record of anatexis.

94

## 95 **2. Geological setting and sampling**

### 96 **2.1 The Velay dome in the French Massif Central**

97 The eastern French Massif Central exposes igneous and metamorphic lithologies  
98 belonging to the inner part of the Variscan belt (Fig. 1), a Devonian–Carboniferous  
99 collisional orogen which resulted from the closure of several oceanic domains and  
100 culminated in the amalgamation of Gondwana, Laurussia and intervening  
101 microcontinents (Matte, 1991). In the eastern French Massif Central, three main  
102 metamorphic nappes have been described (the following description is based on Faure  
103 et al. (2009); Vanderhaeghe et al. (2020) and references therein). The high-grade  
104 *Upper Gneiss Unit* encompasses ortho- and paragneisses, locally anatectic, along with  
105 the so-called Leptynite-Amphibolite Complex interpreted as dismembered ophiolite  
106 fragments. This nappe preserves evidence for an early high-pressure evolution,  
107 records late Devonian to early Carboniferous metamorphic ages and would represent  
108 a crustal segment having experienced continental subduction. It was thrust over the  
109 *Lower Gneiss Unit*, composed of meta-igneous and meta-sedimentary lithologies  
110 which have been pervasively affected by partial melting and intruded by peraluminous  
111 granitic magmas in the late Carboniferous, delineating the Velay migmatite–granite  
112 dome. To the South, the dome is in contact with the *Parautochthonous Unit*, composed  
113 of greenschist to lower amphibolite-facies metasediments. High-grade rocks from the  
114 three units are unconformably sealed by late Carboniferous–early Permian coal-  
115 bearing sediments.

116 The southern Velay dome (Fig. 1) has been the subject of numerous petrological and  
117 geochronological studies reviewed in Barbey et al. (2015). Partial melting took place  
118 under biotite-stable conditions at T of ~720°C and mid-crustal pressures of 0.3–0.6  
119 GPa, locally reaching T ≥ 800°C at P ~ 0.4 GPa (Montel et al., 1992). These higher-T

120 migmatites commonly crop out as diatexites and are spatially related to the Velay  
121 granite s.s (Ledru et al., 2001), dated at 310–300 Ma (Chelle-Michou et al., 2017;  
122 Couzinié et al., 2014; Laurent et al., 2017), and to the main Velay dome emplacement  
123 (Bouilhol et al., 2006; Vanderhaeghe et al., 2020). Other manifestations of this  
124 magmatic event include (Barbey et al., 2015): (i) cross-cutting late intrusive  
125 (micro)granites; (ii) K-rich diorites (locally called "vaugnerites") originating from melting  
126 of the orogenic mantle (Couzinié et al., 2016). Both yielded zircon and monazite U(–  
127 Th)–Pb intrusion ages (ca. 310–295 Ma) that are indistinguishable within uncertainty  
128 from the Velay granite s.s (Couzinié et al., 2014; Didier et al., 2013; Laurent et al.,  
129 2017).

130 Pervasive melting of the middle crust in the Velay dome is tied to the late orogenic  
131 evolution of the Variscan belt (Ledru et al., 2001) and has been attributed to the thermal  
132 maturation of the thickened orogenic crust upon radioactive heating supplemented by  
133 advective heat transfer from mantle- ("vaugnerites") and lower crust-derived magmas  
134 (Barbey et al., 2015; Costa and Rey, 1995; Villaros et al., 2018). The exhumation of  
135 the mid-crustal Velay migmatites and granites was accommodated by: (i) a diapiric  
136 component, revealed by the strain pattern in the dome core; (ii) a strong mechanical  
137 decoupling between the migmatites and the unmelted cover at the roof of the dome,  
138 evidenced by high strain ductile shear zones (Fig. 1) such as the Pilat detachment to  
139 the North or the Mylonitic Metamorphic Vellave Zone (MMVZ) to the South (Bouilhol et  
140 al., 2006).

## 141 **2.2 The Masméjean antiform**

### 142 2.2.1 General outline

143 The Masméjean antiform is a conical structure showing gently dipping southwestern  
144 and northwestern flanks which contrast with the steep eastern flank (Fig. 2). It is built  
145 up by an anatectic orthogneiss core mantled by an association of unmelted  
146 greenschist- to amphibolite-facies orthogneisses and metasediments with very scarce  
147 and small amphibolite bodies. Near Labastide-Puylaurent, the steep N–S foliation of  
148 the eastern flank gradually rotates to an E–W trend, matching that displayed by the  
149 Velay migmatites further East (Bouilhol et al., 2006; Briand et al., 1994; Lapadu-  
150 Hargues, 1947) therefore demonstrating that both domains are in petrological–  
151 structural continuity. Investigation of mineral assemblages in metasediments (Briand

152 et al., 1994; Négron, 1979) led to the recognition of Grt–Chl, And–Bt–Crd and Sil  
153 metamorphic zones (all mineral abbreviations are after Whitney and Evans, 2010), the  
154 close juxtaposition of which defines a low-pressure high-temperature metamorphic  
155 field gradient in the area.

156 Orthogneisses include a range of fine-grained to coarse-grained varieties, some facies  
157 containing K-feldspar porphyroclasts defining an augengneiss texture. They belong to  
158 the Velay Orthogneiss Formation, a peraluminous meta-granite suite regionally defined  
159 as part of the Lower Gneiss Unit, which emplacement was dated at c. 542 Ma  
160 (Ediacaran–Cambrian boundary, Fig. 2, Couzinié et al. (2017)). The metasediments  
161 structurally overlie the orthogneisses or constitute metre- to kilometre-sized rafts  
162 embedded within them. U–Pb dating of detrital zircons constrains their maximum  
163 depositional age to be Ediacaran ( $568.3 \pm 4.9$  Ma, Couzinié et al. (2019)) supporting an  
164 original intrusive contact between the orthogneiss protolith and the (meta)sedimentary  
165 series, later on tectonically transposed. Metamorphic rocks have been intruded: (i) to  
166 the NW by the Margeride granite, dated at  $312.9 \pm 2.0$  Ma (LA–ICP–MS U–Pb zircon,  
167 Laurent et al. (2017)); (ii) to the SE by the Borne granite, dated at  $309.5 \pm 3.6$  Ma (LA–  
168 ICP–MS U–Pb zircon, Couzinié (2017)). Finally, the Masméjean antiform was  
169 unconformably overlain by Lower Jurassic shallow marine limestones upon which  
170 metasediments from the Grt–Chl zone were overthrust at Cenozoic times (Briand et  
171 al., 1994).

### 172 2.2.2 The anatectic core of the antiform

173 One striking field observation in the Masméjean antiform is that migmatites are  
174 exclusively developed at the expense of orthogneisses (Fig. 3a to e). Contrastingly,  
175 paragneisses do not show clear evidence for in situ partial melting. The migmatites  
176 predominantly consist of stromatic metatexites featuring: (i) cm-sized granitic  
177 leucosomes with an assemblage Qz+Pl+Kfs and rare Bt; and (ii) narrow mm-sized  
178 melanosomes consisting of Bt±Ms (Fig. 3f). Biotite is often altered to chlorite and  
179 plagioclase to sericite. Accessory phases include apatite grains (locally mm-sized),  
180 ilmenite, monazite and zircon. Relevant microstructures include (Fig. 3f,g): (i)  
181 interstitial quartz, often dispersed along grain boundaries and locally showing cusped  
182 contacts with adjacent feldspar grains; (ii) well equilibrated quartz–feldspar and  
183 feldspar–feldspar triple junctions. Leucosome concentration within fold hinges (Fig. 3b)  
184 reflects the collection of anatectic liquids in low-strain domains during syn-anatectic

185 deformation. Besides, melt mobility and coalescence is further indicated by the  
186 presence of larger (a few 10's of cm-thick), concordant to discordant granitic  
187 leucosomes (Fig. 3c,d). Those are primarily composed of  $Qz+Pl+Kfs+Bt\pm Ms\pm Sil$  (Fig.  
188 3i). Most migmatites experienced subsolidus deformation as evidenced by undulose  
189 quartz extinction. Finally, scarce vaugnerite bodies have been observed within the  
190 migmatites (Fig. 3e) and are intimately associated with coarse-grained  $Qz$ -feldspar  
191 domains.

### 192 2.2.3 The unmelted parts of the antiform and the contact with the 193 migmatites

194 Metamorphic lithologies from the southwestern flank of the antiform show evidence for  
195 strong ductile deformation involving a combination of pure shear and simple shear (Fig.  
196 2). Marked flattening is supported by: (i) the well-developed foliation associated with  
197 grain-size reduction in augen gneisses and paragneisses, locally grading to S-  
198 mylonites; (ii) the conspicuous occurrence of symmetrical folds the axial planes of  
199 which match the trend of the regional foliation (Fig. 4a). When present, stretching  
200 lineations are underlined by ellipsoidal biotite aggregates and K-feldspars clasts  
201 showing a strong preferential orientation in the YZ plane. They plunge towards the SW  
202 with a maxima at N230 and 21° dip. Sections in the XZ plane reveal C to C' shear  
203 bands, asymmetric drag folds and sigmoid mica "fish" consistently indicative of top-to-  
204 the NE shearing (Fig. 4b). Besides, injected granite bodies in the form of metre- to  
205 hectometre-sized sills are frequently observed in Bt-Sil paragneisses from the lower  
206 part of the high strain zone (Fig. 4c), right above the migmatitic orthogneisses  
207 (corresponding to the so-called "epibolite formation" of Briand et al. (1994), Fig. 2).  
208 Field observations indicate that they intruded before the last increment of top-to-the  
209 NE ductile deformation (Fig. 4d). Finally, non-coaxial deformation along ESE-oriented  
210 (maxima at N110) shear planes evidences a top-to-the S displacement at the brittle-  
211 ductile transition (Fig. 4c). Collectively, these observations strikingly recall the main  
212 features of the Metamorphic Mylonitic Vellave Zone (MMVZ, Bouilhol et al., 2006)  
213 described to the East at the interface between the Velay migmatites and their unmelted  
214 cover (Fig. 1). We therefore conclude that the high-strain zone observed in the SW  
215 flank of the Masméjean antiform represents the western continuation of the MMVZ.

216 In the eastern flank of the antiform, the regional foliation is N-S trending, steeply  
217 dipping towards the E (on average at 55°) and the metamorphic field gradient is even

218 more condensed (Fig. 2). The migmatites are most often overlain by Bt–Sil  
219 paragneisses here again intruded by numerous concordant granite bodies (Lapadu-  
220 Hargues, 1947) grouped together as “Villefort granites” in the following (Fig. 4e). The  
221 And–Bt–Crd zone is notably narrow and its constituent lithologies pervasively affected  
222 by intense ductile deformation, locally resulting in S- and L-mylonites (Fig. 4f).  
223 Stretching lineations are predominantly horizontal and N–S trending, an apparent left-  
224 lateral sense of shear being evidenced by asymmetric quartz aggregates and shear  
225 bands. Ductile structures are overprinted by brittle–ductile and brittle deformation (Fig.  
226 4h and i) along N–S steeply dipping fractures and fault planes with complex kinematics  
227 including both strike-slip and vertical displacements. This high-strain zone is related to  
228 the activity of the so-called “Villefort Shear Zone” which would have been active since  
229 the late Carboniferous (Deroin and Prost, 1993; Lapadu-Hargues, 1947).

230 Finally, in the northwestern part of the antiform, the transition from migmatites to  
231 unmelted rocks appears gradual and there is no evidence for intense ductile shearing  
232 as identified in the other flanks. Stretching lineations are very scarce and, when  
233 present, gently plunge to the NW. Locally, a top-to-the SE sense of shear in unmelted  
234 orthogneisses can be inferred based on asymmetric Kfs clasts. Several metre-thick  
235 granite sills and dykes have been observed both in this area and in the highest  
236 structural levels of the SW flank (in the And–Bt–Crd zone, Fig. 2). Those granites  
237 generally cut across the foliation of unmelted orthogneisses or form concordant bodies  
238 at the interface between meta-igneous and metasedimentary rocks (Fig. 5a to e).

#### 239 2.2.4 Investigated samples

240 A total of 25 samples were studied in this work. The sampling locations (GPS  
241 coordinates) are reported in Supplementary Table S1 and the dated samples are  
242 located on figure 2.

243 Four leucocratic orthogneiss samples (CHA-15-35, -36, -44, -52) were collected from  
244 the And–Bt–Crd zone, two of which (CHA-15-35 and -52) were selected for zircon U–  
245 Pb geochronology. They typically show a planar fabric defined by Ms+Bt layers  
246 alternating with fine- to medium-grained Qz and Pl+Kfs layers, cm-sized Kfs  
247 porphyroclasts being locally present.

248 Seven migmatitic orthogneiss samples were also collected. Sample CHA-15-43 is a  
249 20 cm-thick leucosome within flat-lying metatexites from the antiform core. Sample

250 CHA-15-63 was taken from a decametre-sized granite unit showing gradual contacts  
251 with the surrounding migmatites in the northern part of the antiform. CHA-15-17, CHA-  
252 15-65M and CHA-15-65L (Fig. 3a,d) were all sampled at the Puylaurent dam and  
253 respectively correspond to two bulk metatexites and one leucosome. Besides, two  
254 samples of the Velay migmatites were taken at Saint-Laurent-les-Bains, 6 km east of  
255 the Masméjean antiform (Fig. 2): CHA-15-47 corresponds to a bulk metatexite and  
256 CHA-15-48 a 10 cm-thick leucosome embedded within it.

257 Collected granite samples (13 in total) fall into three groups based on textures,  
258 mineralogy and field relationships:

- 259 - Seven medium-grained, two-mica leucogranites have been collected from  
260 decametre-sized bodies intruding Bt–Sil paragneisses right above the anatectic  
261 core. Five samples (SC14-40, CHA-15-24, -25, -41, -49) correspond to Villefort  
262 granites (from the eastern flank of the antiform). Sample -41 notably displays a  
263 vertical magmatic foliation defined by layers rich in centimetre-sized K-feldspar  
264 crystals alternating with finer-grained leucocratic domains (Fig. 4g). Two  
265 additional samples (CHA-15-05 and -19) have been taken from the SW flank of  
266 the antiform (Fig. 4c). All samples underwent sub-solidus high-temperature  
267 deformation witnessed by sub-grain rotation in quartz and the presence of Ms-  
268 and Sil-filled shear bands. Locally, sample -41 features mm-scale cataclastic  
269 bands showing marked grain-size reduction and subsequent alteration (Fig. 4h).  
270 Retrogression is evidenced by the replacement of biotite by chlorite and  
271 plagioclase by sericite (Fig. 4i).
- 272 - Samples CHA-15-29, -34, -51 and -59 are pink two-mica granite dykes cutting-  
273 across the foliation of unmelted orthogneisses and metasediments within the  
274 Crd–Bt–And zone (Fig. 5a,b,e). Sample CHA-15-51 contains garnet. All  
275 samples experienced subsolidus deformation, from weak (Qz undulose  
276 extinction; CHA-15-34, -51) to marked (Qz subgrain rotation; CHA-15-29, -59).
- 277 - Samples CHA-15-33 and -07 have been taken from metre-sized sills concordant  
278 within the foliation of the orthogneisses and metasediments in the And–Bt–Crd  
279 zone. They are fine-grained porphyritic biotite granites displaying a magmatic  
280 fabric defined by the planar orientation of mm-sized embayed quartz and  
281 feldspar phenocrysts along with biotite aggregates, particularly abundant in

282 sample -07 (Fig. 5c,d). CHA-15-33 also contains magmatic muscovite  
283 phenocrysts.

284

### 285 **3. Analytical and modelling techniques**

#### 286 **3.1 Whole-rock geochemistry**

287 Whole-rock chemical compositions of the selected samples were obtained from the  
288 *ALS Global* company, combining ICP–AES and ICP–MS analyses for major and trace  
289 elements, respectively, and plotted using the GCDkit software (Janoušek et al., 2006).  
290 Results are presented in Supplementary Table S1 and summarized in figures 6 and 7.

#### 291 **3.2 Zircon U–Pb dating**

292 Zircon grains were separated from 17 crushed rock samples at Saint-Etienne  
293 University using conventional techniques (sieving, panning, magnetic and heavy  
294 liquids separation followed by handpicking). Selected grains were subsequently cast  
295 into epoxy mounts and polished down to an equatorial section. Back-scattered electron  
296 (BSE) and cathodoluminescence (CL) imaging were performed at the Central  
297 Analytical Facility of Stellenbosch University (SUN, South Africa) using a Zeiss  
298 MERLIN scanning electron microscope (SEM) and at the Laboratoire Magmas et  
299 Volcans (Clermont-Ferrand) using a Jeol JSM-5910 SEM. Analyses of U–Pb isotopes  
300 were carried out by laser ablation – inductively coupled plasma – sector-field – mass  
301 spectrometry (LA–ICP–SF–MS) at Goethe Universität, Frankfurt-am-Main (GUF,  
302 Germany) and at ETH Zurich (Switzerland), in both cases via a RESOLUTION  
303 (ASI/Applied Spectra, Australia/USA) excimer (ArF, 193 nm) laser ablation system  
304 attached to an Element XR (Thermo, Germany) ICP-MS. Detailed information about  
305 the analytical methods are presented in the Supplementary Text, including the  
306 methodology followed to propagate systematic errors to the calculated Concordia  
307 dates. The full analytical datasets (standards and samples) are reported in  
308 Supplementary Tables S2 to S5. The CL image of each zircon grain along with the  
309 location of the laser spots and associated U–Pb data are displayed Supplementary  
310 Figures S1 to S5. A summary of the main texture–date results is provided Figure 8 and  
311 results of U-Pb analyses summarized in Figure 9 (for orthogneisses and migmatites)  
312 and Figure 10 (for granites).

### 313 **3.3 Phase relations and trace-element modelling**

314 Forward thermodynamic modelling was performed in order to investigate the P–T–X<sub>H<sub>2</sub>O</sub>  
315 conditions of anatexis in the Masméjean antiform. Field observations and migmatite  
316 U–Pb zircon data (see section 4.2) indicate that augen gneisses from the Velay  
317 Orthogneiss Formation arguably constitute the protolith of the migmatites. Accordingly,  
318 a representative unmelted augen gneiss composition was chosen as starting  
319 composition (SC-14-33, from Couzinié et al. (2017)). Pseudosections were calculated  
320 by Gibbs energy minimization using PerpleX (Connolly, 2009) and the self-consistent  
321 thermodynamic dataset of Holland and Powell (1998) (updated version of 2004) in the  
322 system Na<sub>2</sub>O–CaO–K<sub>2</sub>O–FeO–MgO–Al<sub>2</sub>O<sub>3</sub>–SiO<sub>2</sub>–H<sub>2</sub>O–TiO<sub>2</sub> (NCKFMASHT). The  
323 selected solution models are listed in the Supplementary Text. The starting  
324 composition was recalculated anhydrous and the H<sub>2</sub>O concentration subsequently set  
325 at 0.53 wt.%, based on a T–X<sub>H<sub>2</sub>O</sub> pseudosection, to obtain a fully hydrated subsolidus  
326 system at 0.5 GPa. The retained chemical composition is displayed Table 1. Following  
327 the methodology of Janoušek and Moyen (2019), the Rb, Ba, Sr and Nb contents of  
328 modelled melts and solid residues were estimated at 63 points within the modelled P–  
329 T–X<sub>H<sub>2</sub>O</sub> sections (between 680–800°C at 0.4–0.6 GPa and for bulk water contents of  
330 0.53, 1.6 and 2.6 wt.%, Fig. 11a,b) using: (i) the calculated major element melt  
331 compositions and phase proportions; (ii) a set of partition coefficients for felsic systems  
332 compiled by Laurent et al. (2013) and listed Supplementary Table S6.

333

## 334 **4. Results**

### 335 **4.1 Geochemistry**

#### 336 4.1.1 Orthogneisses

337 Geochemical data from investigated orthogneisses were merged with the existing  
338 dataset available for the Velay Orthogneiss Formation (Couzinié et al., 2017) in the  
339 study area. The constituent augen gneisses (n=10) and leucogneisses (n=11)  
340 correspond to metamorphosed porphyritic granites and leucogranites, respectively,  
341 with SiO<sub>2</sub> contents ranging from 69.4 to 78.6 wt.%. Together, they define a  
342 peraluminous, potassic (K/(Na+K): 0.49–0.59) and ferriferous association (sensu  
343 Debon and Le Fort (1988), Fig. 6). Augen gneisses show moderate LILE (Sr: 60–141  
344 ppm; Ba: 356–1140 ppm, Fig. 7) and elevated HFSE (Zr: 110–234 ppm; Nb: 7.9–13.5

345 ppm) and REE (Sum of REE: 88–150 ppm) contents along with moderately  
346 fractionated REE patterns ( $La_N/Yb_N$ : 4–9) and negative Eu anomalies ( $Eu_N/Eu^*$ : 0.33–  
347 0.82, Fig. 7). Detailed description and interpretation of the geochemical signature of  
348 this meta-igneous suite are presented in Couzinié et al. (2017).

#### 349 4.1.2 Migmatites

350 The three metatexites mostly overlap in terms of major and trace element composition  
351 with unmelted augen gneisses (Fig. 6, 7). The melanocratic sample CHA-15-65M is  
352 less silicic but more potassic, mafic and richer in Nb (up to 14.9 ppm) which reflects a  
353 higher modal abundance of biotite (Bea et al., 1994; Debon and Le Fort, 1988).

354 The leucosomes are highly silicic ( $SiO_2$ : 72.6–76.3 wt.%), peraluminous and potassic  
355 ( $K/(Na+K)$ : 0.52–0.61, Fig. 6). They show LILE contents (Sr: 54–85 ppm; Ba: 147–526  
356 ppm) similar to those of augen gneisses but are markedly depleted in HFSE (Zr <42  
357 ppm, Nb <7.5 ppm) and REE (Sum<sub>REE</sub> <46 ppm, Fig. 7a). REE patterns are poorly  
358 fractionated ( $La_N/Yb_N$ : 1.7–5.3) and Eu anomalies ranging from slightly negative to  
359 slightly positive (Fig. 7,  $Eu_N/Eu^*$ : 0.79–1.15) apart from sample 43 ( $Eu_N/Eu^*$  = 0.35).

#### 360 4.1.3 Granites

361 Granites are peraluminous and define a trend with a positive slope between the felsic  
362 and high peraluminous fields in the B–A diagram. They overall share similar major  
363 element compositions with meta-granites from the Velay Orthogneiss Formation but  
364 are slightly more magnesian (Fig. 6). The granite dataset can be divided into two  
365 groups based on whole-rock geochemistry.

366 A first group termed “low-Ba granites” encompasses three dykes (CHA-15-29, -34, -  
367 51) from the And–Crd–Bt zone and two Villefort granites (CHA-15-24, -25). These  
368 samples are leucogranites s.s., highly silicic ( $SiO_2$ : 72.6–75 %), sodi-potassic to sodic  
369 ( $K/(Na+K)$ : 0.39–0.50, Fig. 6b), and strongly depleted in LILE (Sr <60 ppm; Ba <170  
370 ppm) compared to the leucosomes (Fig. 7). HFSE and REE contents are markedly low  
371 (Zr <30 ppm; Sum of REE <50 ppm) apart from Nb (6.8–16.3 ppm). They display poorly  
372 fractionated REE patterns ( $La_N/Yb_N$ : 3–7) with marked Eu negative anomaly ( $Eu_N/Eu^*$ :  
373 0.35–0.56, Fig. 7).

374 A second group termed “high-Ba granites” includes dyke CHA-15-59, the fine-grained  
375 porphyritic granite sills (CHA-15-07 and -33) and remaining bodies intrusive within Bt–  
376 Sil-paragneisses (CHA-15-05, -19, -41, -49, -59, SC-14-40). They show a broader

377 range of SiO<sub>2</sub> contents (66–74 wt.%) and are more potassic than the “low-Ba” granites  
378 (K/(Na+K): 0.52–0.69). They are richer in LILE (Sr: 103–279 ppm; Ba: 390–1310 ppm)  
379 and Zr–REE (Zr: 81–228 ppm; Sum<sub>REE</sub>: 80–178 ppm) than low-Ba granites and  
380 leucosomes. Nb contents are similar to low-Ba types (11–17.4 ppm). REE patterns are  
381 fractionated (La<sub>N</sub>/Yb<sub>N</sub>: 9–29) and feature a moderate negative Eu anomaly (Eu<sub>N</sub>/Eu\*:  
382 0.41–0.73).

## 383 4.2 Zircon U–Pb dates

### 384 4.2.1 Orthogneisses

385 Zircon grains extracted from orthogneiss samples are euhedral to sub-euhedral, range  
386 in size from 80 to 400 μm, display aspect ratios between 1.4:1 and 3:1 and show well-  
387 developed {2 1 1} pyramids (Fig. 8a). Core–rims relationships are common and  
388 typically feature CL-dark cores (most often poorly zoned and sometimes recrystallized)  
389 surrounded by rims with well-developed magmatic oscillatory zoning. Grains devoid of  
390 cores generally show a similar, oscillatory zoning pattern. Such rims and  
391 homogeneous grains yielded Concordia dates of 544.1 ± 4.9 Ma (MSWD<sub>C+E</sub>=0.79,  
392 n=11) and 544.4 ± 5.2 Ma (MSWD<sub>C+E</sub>=0.9, n=9) for CHA-15-35 and CHA-15-52,  
393 respectively (Fig. 9), together with low Th/U ratios (average of 0.15). In both samples,  
394 few measurements yielded a range of younger, nearly concordant, <sup>206</sup>Pb/<sup>238</sup>U dates  
395 down to 514 ± 7 Ma. Analyses performed on zircon cores and additional core-free  
396 grains mostly yielded concordant Neoproterozoic (700–560 Ma) dates. Some  
397 discordant analyses in both samples showed similar <sup>206</sup>Pb/<sup>238</sup>U as concordant spots  
398 but higher <sup>207</sup>Pb/<sup>206</sup>Pb (Fig. 9), attributed to the presence of common Pb.

### 399 4.2.2 Migmatites

400 Zircon crystals extracted from the metatexites and leucosomes are very similar in  
401 sizes, shapes and internal textures to orthogneiss zircons. In metatexite CHA-15-17,  
402 zircon grains tend to be more elongated (aspect ratios up to 5.5:1, Fig. 8) and  
403 commonly lack inherited cores. Besides, zircons are notably smaller (mostly <90 μm)  
404 in leucosome CHA-15-63 (Fig. 8). Results of U–Pb dating were very consistent from  
405 one sample to another. Concordant <sup>206</sup>Pb/<sup>238</sup>U dates obtained on oscillatory-zoned  
406 core-free grains and rims clustered in the range 550–540 Ma (Fig. 9) and showed low  
407 Th/U ratios (average 0.12). Concordia dates of 545.1 ± 4.8 Ma (MSWD<sub>C+E</sub>=1.02, n=16),  
408 539.7 ± 5.7 Ma (MSWD<sub>C+E</sub>=1.3, n=4) and 549.0 ± 4.8 Ma (MSWD<sub>C+E</sub>=1.04, n=14) can

409 be calculated for metatexites from the Velay (CHA-15-48) and the Masméjean antiform  
410 (CHA-15-17 and -65M), respectively. Cores and few core-free crystals yielded older,  
411 predominantly Cryogenian–Ediacaran dates (>560 Ma). No concordant zircon date  
412 was retrieved for leucosome sample CHA-15-65L.

413 In the leucosomes, two groups of zircon grains deserve special attention as they did  
414 not yield any reliable U–Pb date because they exhibited complex and irregular isotope  
415 fractionation patterns during ablation (labelled “ns” in Supplementary Figures, for which  
416 no date could be calculated), or showed a scattered range of highly (>50%) discordant  
417 Permian to Jurassic  $^{206}\text{Pb}/^{238}\text{U}$  dates. In both cases, the spotted grains were very rich  
418 in common Pb. Such zircon grains belong to two textural types: short CL-dark to bright  
419 oscillatory zoned core-free grains, particularly abundant in sample CHA-15-65L; and  
420 CL-dark porous metamict rims wrapping 650–540 Ma CL-bright zoned cores (Fig. 8,  
421 rather present in CHA-15-43 and CHA-15-47).

#### 422 4.2.3 Granites

423 Zircon grains from both low- and high-Ba granite samples are similar. They are  
424 generally euhedral and show a broad range of sizes (60–350  $\mu\text{m}$ ) and aspect ratios  
425 (1.1:1–3.6:1), up to 6:1 in sample CHA-15-19. Three zircon types can be recognized  
426 (Fig. 8). A first, scarce type corresponds to grains featuring a CL-dark or bright  
427 occasionally zoned core, truncated by a new growth zone with distinct magmatic  
428 oscillatory zoning, similar to zircons extracted from orthogneisses. Concordant  
429  $^{206}\text{Pb}/^{238}\text{U}$  dates obtained from cores and rims were almost exclusively pre-Variscan,  
430 predominantly Ediacaran. A second, abundant type encompasses grains with  
431 oscillatory zoned cores wrapped by CL-dark porous rim, often <15  $\mu\text{m}$ -large and  
432 sometimes displaying faint oscillatory zoning. Analyses of the largest rims revealed  
433 high common Pb contents, low Th/U (<0.1) and very few gave concordant Variscan U–  
434 Pb dates, often after a common Pb correction was performed. A third group  
435 corresponds to zircon grains devoid of core–rim relationships and showing well-  
436 developed magmatic oscillatory zoning. Most of them also yielded pre-Variscan  
437 (mostly Ediacaran) dates but concordant Variscan were obtained on some grains  
438 typified by elevated Th/U ratios (mostly in the range 0.4–1.2).

439 Most analyses performed on the four “low-Ba” granites (CHA-15-24, -25, -34 and -51)  
440 yield  $^{206}\text{Pb}/^{238}\text{U}$  dates clustered around ca. 550–540 Ma, with few (notably from cores)

441 older (mostly Ediacaran–Cryogenian) dates (Fig. 10). Only three analyses yielded  
442 concordant Variscan dates, all from sample CHA-15-24 for which the Concordia date  
443 of  $305.8 \pm 4.4$  Ma ( $\text{MSWD}_{\text{C+E}}=1.5$ ,  $n=3$ ) can be calculated. The same situation is  
444 observed for the “high-Ba” granites with a dominant Ediacaran population (except in  
445 sample CHA-15-19 and -49) and scarce Variscan dates, albeit more frequent than in  
446 the “low-Ba” types. Concordia dates of  $304.0 \pm 3.9$  Ma ( $\text{MSWD}_{\text{C+E}}=1.4$ ,  $n=5$ ),  $305.3 \pm 3.9$   
447 Ma ( $\text{MSWD}_{\text{C+E}}=0.6$ ,  $n=5$ ) and  $302.2 \pm 3.7$  Ma ( $\text{MSWD}_{\text{C+E}}=1.6$ ,  $n=6$ ) can be calculated  
448 for CHA-15-41, CHA-15-19 and CHA-15-33, respectively. One single grain from  
449 sample CHA-15-49 yielded a Variscan concordant  $^{206}\text{Pb}/^{238}\text{U}$  date of  $305 \pm 4$  Ma.

## 450 5. Discussion

### 451 5.1 Interpretation of U–Pb dates

452 For *orthogneisses*, identical (igneous) zircon textures, Th/U ratios and U–Pb dates  
453 have been reported by Couzinié et al. (2017) on similar rocks from the southern part  
454 of the Velay dome. Following this, we interpret the Concordia dates of  $544.1 \pm 4.9$  Ma  
455 and  $544.4 \pm 5.2$  Ma obtained for CHA-15-35 and CHA-15-52 as the crystallization ages  
456 of their granitic protoliths. As they were obtained on texturally and compositionally  
457 similar crystals, the range of slightly younger  $^{206}\text{Pb}/^{238}\text{U}$  dates would represent isotopic  
458 resetting possibly related to the Variscan thermal event and/or recent Pb loss. Zircon  
459 domains showing older dates (Paleoproterozoic and Neoproterozoic) would  
460 correspond to source-inherited grains or xenocrysts incorporated from Ediacaran  
461 sedimentary country-rocks during magma ascent.

462 For *granites*, we interpret the Concordia dates of  $305.8 \pm 4.4$ ,  $304.0 \pm 3.9$ ,  $305.3 \pm 3.9$ ,  
463 and  $302.2 \pm 3.7$  Ma obtained on (rare) rims as the crystallization ages of samples CHA-  
464 15-24 (“low-Ba”), -41, -19 and -33 (“high-Ba”), respectively. Notably, Variscan dates  
465 were obtained from zircon rims and crystals having textural characteristics (CL-dark,  
466 faintly zoned) contrasting with zircon grains (domains) with pre-Variscan dates (Fig.  
467 8d). The latter would have been inherited from the source or incorporated during ascent  
468 from country-rocks. Importantly, inherited grains constitute the bulk of the zircon  
469 budget of four granite samples (CHA-15-24, -34, -49 and -51), for which no  
470 crystallization age can be estimated.

471 The zircon grains extracted from the *metatexites* show similar CL characteristics, Th/U  
472 ratios and  $^{206}\text{Pb}/^{238}\text{U}$  dates than those of the local unmelted orthogneisses. The

473 Ediacaran ( $549.0 \pm 4.8$  to  $539.7 \pm 5.7$  Ma) Concordia dates are therefore interpreted  
474 as reflecting the crystallization age of the granitic protolith of the migmatites. Similarly,  
475 the distribution of zircon dates in the **leucosomes** clusters in the range 550–540 Ma  
476 and remarkably mimics that of the orthogneisses and metatexites (Fig. 11a). Even  
477 though such dates were obtained on grain domains showing well-developed oscillatory  
478 zoning, we argue that they do not correspond to the leucosome crystallization ages.  
479 Indeed, Bouilhol et al. (2006) report the occurrence of magmatic monazite grains and  
480 overgrowths of late Carboniferous age in leucosomes (as constrained by “chemical”  
481 U–Th–Pb dating), which indicates that melt production and coalescence took place at  
482 Variscan times, as observed throughout the Velay dome. Consequently, in the  
483 Masméjean migmatites, the age of the anatectic event is not recorded by zircon.

484 Many zircon analyses in the leucosomes and granites yielded highly discordant dates  
485 or unusual laser-induced Pb/U fractionation patterns. Such disturbance of the U–Pb  
486 system likely results from Pb loss and/or common Pb incorporation related either to  
487 radiation-induced damage for the metamict domains (Mezger and Krogstad, 1997;  
488 Nasdala et al., 1998) or crystallization from volatile-rich melts (Watson et al., 1997).

489 Two main conclusions can be drawn from this dataset. First, both “low-Ba” and “high-  
490 Ba” granites would be coeval within uncertainties ( $\pm 4$  Ma) and were emplaced at c. 304  
491 Ma. Their abundant inherited/xenocrystic zircon grains show a unimodal distribution of  
492  $^{206}\text{Pb}/^{238}\text{U}$  dates featuring a marked peak at c. 545 Ma (Fig. 11b and c) as already  
493 described in several Velay granites (Chelle-Michou et al., 2017; Couzinié et al., 2014;  
494 Laurent et al., 2017). Assuming that most xenocrysts were incorporated in the magma  
495 at source level, the perfect match with the emplacement ages of orthogneisses  
496 indicates that the latter constitute the source of both “low-Ba” and “high-Ba” granite  
497 magmas. The presence of 680–560 Ma-old dates may record the subordinate  
498 involvement of metasediments since this age range represents the main detrital zircon  
499 population in the latter (Couzinié et al., 2019). However, most of the pre-545 Ma zircon  
500 domains actually correspond to cores wrapped by c. 545 Ma-old rims, suggesting they  
501 were already incorporated as inherited grains in the granite protolith of the  
502 orthogneisses.

503 Second, the zircon record of Variscan crustal melting in the Masméjean antiform is  
504 strikingly limited. Notably, none of the studied metatexites ( $n = 3$ ) and leucosomes ( $n$   
505  $= 4$ ) record any Variscan date (even discordant), and only half of the dated granites

506 yield unambiguous evidence for zircon crystallization during the regional Carboniferous  
507 thermal event. In total, out of 494 analyzed zircon grains, only 20 yielded concordant  
508 Variscan  $^{206}\text{Pb}/^{238}\text{U}$  dates, of which 11 after a common Pb correction only. In other  
509 words, <2% of our dataset yielded pristine dates corresponding to the Variscan partial  
510 melting event. The significance of this is discussed section 5.5.

## 511 **5.2 P–T– $X_{\text{H}_2\text{O}}$ conditions of melting**

512 Following petrographic observations (see section 2), the paragenesis inferred at peak  
513 metamorphic conditions for the migmatites is: melt+Qz+Kfs+Pl+Bt $\pm$ Sil $\pm$ Ms.  
514 Examination of the pseudosection calculated for a representative orthogneiss  
515 composition fully hydrated at the solidus, i.e. with 0.53 %  $\text{H}_2\text{O}$  (see section 3.3),  
516 indicates that the stability field of this mineral assemblage is bounded at low  
517 temperature by the solidus and at high temperature (and/or low pressure) by biotite-  
518 breakdown and associated appearance of garnet and/or cordierite (Fig. 12a). As these  
519 two minerals have not been observed in the migmatites, partial melting in the  
520 Masméjean dome would have taken place at  $0.3 < P < 0.7$  GPa and  $650 < T < 720^\circ\text{C}$ ,  
521 consistent with the estimates of Montel et al. (1992). Importantly, at these P–T  
522 conditions muscovite dehydration-melting would be the main melt-producing reaction,  
523 generating sillimanite and K-feldspar as peritectic phases (Clemens and Vielzeuf,  
524 1987; Patiño Douce and Harris, 1998). However, with the low  $X_{\text{H}_2\text{O}}$  considered in the  
525 protolith (0.53 wt.% at near-solidus conditions), as little as 2–5 vol.% melt would have  
526 been produced by muscovite-dehydration melting only (Fig. 12a).

527 Clearly, such estimates are inconsistent with field observations which evidence melt  
528 mobility at the metre scale (Fig. 3), and likely over 100's of metres or about a kilometre,  
529 considering that the granite sheets intruding the lower-grade metasediments and  
530 orthogneisses stem from deeper parts of the same migmatite zone (as supported by  
531 zircon U–Pb data). This indicates that the likely melt fraction was between the melt  
532 percolation threshold under strain of 7 vol.% (Rosenberg and Handy, 2005) and the  
533 static melt escape threshold of 20–25 vol.% (Vigneresse et al., 1996). A T– $X_{\text{H}_2\text{O}}$   
534 pseudosection (Fig. 12b) highlights that the melt volumes inferred (roughly 10–20  
535 vol.%) can be readily explained by a bulk  $\text{H}_2\text{O}$  content of c. 1–2 wt.%. This is  
536 significantly higher than the amount of water required to fully hydrate the orthogneiss  
537 protolith (0.53 wt.%), which therefore requires water ingress at near- or supra-solidus

538 conditions. Elevated  $X_{H_2O}$  in the bulk composition does not affect the main mineral  
539 assemblages at given T but results in a dramatic increase of the melt productivity (Fig.  
540 12b) due to the "eutectic" composition of the orthogneiss source, with quartz and  
541 feldspars being dissolved in the melt phase via the reaction  $Qz + Kfs + Pl + H_2O =$   
542 melt, only limited by water availability (Johannes and Holtz, 1996).

543 Further evidence for low-temperature water-fluxed melting in the Masméjean  
544 orthogneisses is provided by the examination of the overlying Bt–Sil paragneisses from  
545 the high-strain zone (MMVZ). These rocks are in direct contact with the anatectic  
546 orthogneisses (cf. "melt-in" domain, Fig. 2), regionally experienced the same peak  
547 temperatures of 680–710°C (Bouilhol et al., 2006) and yet do not show clear evidence  
548 for partial melting. A T– $X_{H_2O}$  pseudosection calculated for a representative paragneiss  
549 (SC-14-41) shows that melt productivity in such rocks is not affected by water ingress  
550 at  $T < 730^\circ\text{C}$  (Fig. 12c,d). This feature likely reflects the near absence of K-feldspar in  
551 the paragneisses at peak metamorphic conditions (Négron, 1979), hampering  
552 substantial melt production by the "eutectic" melting reaction. In the paragneisses, K-  
553 feldspar is therefore the limiting reactant, and not  $H_2O$  as in the peraluminous  
554 orthogneiss which were able to produce 10–20 vol% of melt as a result of water fluxing  
555 in the same conditions.

### 556 **5.3 Interpretation of granite geochemistry**

557 Field relationships and zircon U–Pb systematics of Variscan leucosomes, "low-Ba" and  
558 "high-Ba" granites from the Masméjean antiform indicate that all rock types represent  
559 magmas produced by melting of an orthogneiss source. In this section, we unravel the  
560 petrogenetic processes accounting for their contrasting whole-rock major and trace  
561 element compositions.

562 Comparison between equilibrium melt compositions predicted by thermodynamic  
563 modelling and natural samples are consistent for the "low-Ba" granites and leucosome  
564 CHA-15-43 (Fig. 13a). Both their normative feldspar–quartz proportions and Ba–Sr–  
565 Rb–Nb concentrations match that of modelled primary melts extracted from an average  
566 augen gneiss at  $T < 760^\circ\text{C}$  (based on Ba–Nb systematics) and under a large range of  
567  $X_{H_2O}$  (Fig. 13b and c). Low melting temperatures are also supported by their low  
568 contents in REE, Th and Zr because these chemical elements are hosted in accessory  
569 minerals (monazite, zircon) which solubilities in melts are positively correlated with

570 temperature (Rapp and Watson, 1986; Watson and Harrison, 1983). Monazite  
571 saturation thermometry, which is more robust than zircon saturation thermometry due  
572 to the higher solubility of monazite in peraluminous melts compared to zircon (Kelsey  
573 et al., 2008), points to melt temperatures of 645–705°C (using the model of Montel  
574 (1993)). Collectively, modelling results and saturation thermometry indicate that the  
575 “low-Ba” granites would adequately represent equilibrium anatectic melts extracted  
576 from the migmatites exposed in the core of the Masméjean antiform.

577 Most leucosomes depart from the composition of “low-Ba” granites, being richer in Or–  
578 Q components (Fig. 13a), displaying lower Nb and higher Ba–Sr (Fig. 13b,c) contents  
579 and lacking significant Eu anomaly (Fig. 7a). A simple model of 20% accumulation of  
580 K-feldspar (Fig. 13c) can account both for their potassic character and the excess Ba–  
581 Sr–Eu (elements hosted in the accumulated feldspar). However, their highly variable  
582 and distinctly lower Nb contents, inconsistent with values predicted by equilibrium  
583 melting of the orthogneisses, cannot be explained solely by K-feldspar accumulation.  
584 One way to achieve such low concentrations would be to consider the role of  
585 disequilibrium processes during partial melting (Johannes, 1983). When mineral  
586 reactants in the melting reaction are consumed, they release their trace element  
587 budget to the melt. Then, the trace elements equilibrate with the solid residue by  
588 diffusion based on partition coefficients. If equilibration is not attained, the melt leaves  
589 the source with a trace element composition governed by the stoichiometry of the  
590 mineral reactants. In the Masméjean migmatites, biotite is not involved in the melting  
591 reaction and the very first melts formed are likely to be strongly depleted in Nb (Fig.  
592 13b). Considering the results of monazite saturation thermometry (632–697°C), the  
593 leucosomes would therefore represent low temperature melts having failed to fully  
594 equilibrate with the biotite-rich residuum (explaining their low Nb contents) and  
595 encompassing a load of relict source crystals (mostly K-feldspar).

596 The “high-Ba” granites are poorer in SiO<sub>2</sub>, richer in K<sub>2</sub>O and slightly more mafic than  
597 leucosomes and “low-Ba” granites (Fig. 6, 13). Results of peraluminous orthogneiss  
598 melting experiments (Castro et al. (1999); García-Arias et al. (2012); Fig. 6) indicate  
599 that such features can be primarily ascribed to higher melting temperatures ( $T \geq 780^\circ\text{C}$ ),  
600 reaching those required for substantial biotite breakdown. Elevated melting  
601 temperature are also supported by their high LREE contents with monazite saturation  
602 thermometry yielding 760–822°C. Sample CHA-15-07 is more mafic than experimental

603 melts (Fig. 6) which can be related to the presence in the sample of abundant mm-  
604 thick biotite aggregates (see section 2.2.4) of possible xenocrystic origin. Importantly,  
605 Ba–Sr contents are markedly higher than predicted by the high-T melting model (Fig.  
606 13b) and cannot result from the accumulation of K–feldspar and plagioclase as this  
607 would require unrealistic high amounts of cumulative feldspar (>30 wt.%, Fig. 13c).  
608 Considering a diffusional disequilibrium melting model (as advocated for the  
609 leucosomes), the positive correlation between Nb and Ba contents (Fig.13b) could  
610 result from the concomitant dissolution of plagioclase, K-feldspar and biotite into the  
611 melt phase without diffusive equilibration with the solid residue, the least equilibrated  
612 melts showing the highest Ba–Nb. This trend is anchored in the compositional field of  
613 high-T melts generated under elevated  $X_{H_2O}$  suggesting that the “high-Ba” granite  
614 magmas could also have formed through water-fluxed melting but at temperatures  
615 markedly higher than the “low-Ba” granites and leucosomes (800°C instead of 700°C).

#### 616 **5.4 Timing of anatexis and origin of the fluxing water**

617 From East to West, the architecture of the contact between the dome and the overlying  
618 metamorphic series evolves from overturned to the south (Burg and Vanderhaeghe  
619 (1993) to nearly vertical in the Saint-Laurent-les-Bains cross-section (Fig. 2, Bouilhol  
620 et al., 2006). This geometry reflects the dome emplacement dynamics at different  
621 structural levels (deeper to the East). As such, a schematic pre-doming restored  
622 section across the SW part of the Velay dome is depicted figure 14. From this  
623 perspective, the MMVZ can be regarded as a relatively flat-lying shear zone the  
624 development and activity of which was, based on field observations (see section 2.2),  
625 contemporaneous with water-fluxed melting and granite magmatism. The fact that both  
626 “low-Ba” and “high-Ba” granite types coexist and yield crystallization ages that are  
627 identical within uncertainty suggests that they are the products of the same melting  
628 event but sample different depths within the crust (Fig. 14). Specifically, the “low-Ba”  
629 granites represent anatectic melts extracted from low-T migmatites (700°C)  
630 corresponding to those observed at the present exposure level, while the “high-Ba”  
631 hotter (800°C) granites stem from maximum a few km deeper. The timing of magma  
632 production, segregation from the source, ascent and crystallization is generally in the  
633 order of a few million years (Harris et al., 2000; Petford et al., 2000), i.e. comparable  
634 to or smaller than the typical dating uncertainties obtained here for granites (about  $\pm 4$   
635 Ma). Therefore, the crystallization ages obtained for both the “low-Ba” and “high-Ba”

636 granites can be reasonably considered as dating the anatexis event. Hence, water-  
637 fluxed melting in the Masméjean antiform most likely took place within the time interval  
638 310–300 Ma and was followed by fast cooling as evidenced by the crystallization age  
639 of  $302.2 \pm 3.7$  Ma obtained on the fine-grained granite CHA-15-33 which arguably was  
640 emplaced at shallow crustal levels in an already cooled basement.

641 The origin of water which fostered orthogneiss melting in the Masméjean antiform  
642 remains elusive. Three sources may be considered: (i) meteoric water, percolating  
643 down to the middle crust (Wickham and Taylor, 1985); (ii) metamorphic water  
644 originating from the dehydration of deeper-lying or underthrust rocks (Sawyer, 2010),  
645 (iii) magmatic water conveyed by hydrous melts (Weinberg and Hasalová, 2015).  
646 Evidence for case (i) is very scarce in the geological record (see review in Weinberg  
647 and Hasalová (2015)). Meteoric water infiltration down to depths of at least 3 km has  
648 been documented within late orogenic shear zones elsewhere in the Variscan belt  
649 (Dusséaux et al., 2019), but the melting pressure of  $>0.3$  GPa (i.e.  $>11.5$  km,  
650 considering an average crustal density of  $2700 \text{ kg.m}^{-3}$ ) inferred for the Masméjean  
651 antiform (see section 5.2) makes such a fluid source unlikely. Considering case (ii), the  
652 local thermal structure implies that crustal rocks underlying the Masméjean antiform  
653 were also at supra-solidus conditions. Therefore, any metamorphic water released  
654 upon heating at deeper crustal levels would have been instantaneously dissolved in a  
655 granitic melt phase (Sawyer, 2010) and was thus unable to trigger melting at higher  
656 crustal levels.

657 Ascent of hydrous granitic melts followed by diffusive transfer of magmatic  $\text{H}_2\text{O}$  along  
658 chemical potential gradients at the emplacement site has been recently invoked to  
659 explain water-fluxed melting (Tafur and Diener, 2020; Weinberg and Hasalová, 2015).  
660 Villaros et al. (2018) argued that the intrusion of  $\text{H}_2\text{O}$ -rich granitic melts ( $X_{\text{H}_2\text{O}} > 8$  wt.%)  
661 generated at pressures in excess of 1 GPa was responsible for water-fluxed melting of  
662 orthogneisses in the Velay dome. Such a model is plausible but difficult to prove based  
663 on field observations in the Masméjean antiform. Indeed, the only evidence for the  
664 percolation of granitic melts in the molten domain is represented by the discordant  
665 leucosomes which, based on petrographic, geochemical and geochronological data,  
666 most likely represent magmas derived from the local orthogneisses. However, it  
667 remains possible that the “wet” granitic melts of Villaros et al. (2018) were emplaced  
668 and induced melting below the current level of exposure (Fig. 14).

669 Water-fluxed orthogneiss melting could also result from the ingress of magmatic water  
670 exsolved following the crystallization of the high-K diorites (“vaugnerites”) exposed in  
671 the Masméjean antiform (and throughout the Velay dome). Indeed, the solidus of the  
672 high-K diorites lies at about 800°C and their parental magmas were H<sub>2</sub>O-rich (Montel  
673 and Weisbrod, 1986; Parat et al., 2009) meaning that they were able to release a  
674 supercritical H<sub>2</sub>O-rich fluid at temperatures close to that inferred for the genesis of the  
675 Masméjean granites–migmatites. The volumes of high-K diorites at the current  
676 exposure level are limited but the presence of larger bodies at depth can be expected  
677 since dioritic magmas are involved in the petrogenesis of the two nearby and coeval  
678 granite batholiths (the c. 310 Ma Margeride and Borne plutons, Moyen et al. (2017)).

### 679 **5.5 The scant zircon record of water-fluxed orthogneiss melting**

680 As shown earlier (section 5.1), a striking feature of the U–Pb zircon dataset is the  
681 complete absence of Variscan dates in the migmatites (bulk metatexites and  
682 leucosomes). Some grain rims may have crystallized from the newly formed melt  
683 fraction but this cannot be ascertained, either because these rims were too small for  
684 analysis with routine dating procedures (specialized sample preparation and analytical  
685 conditions allowing depth profiling, e.g. Campbell et al. (2005), may allow to date such  
686 thin rims), or because they did not yield reliable U–Pb dates (see section 4). Only one  
687 “low-Ba” granite sample, arguably corresponding to an anatectic melt extracted from  
688 the migmatites, yielded three Variscan dates. In this section, we examine several  
689 parameters that could explain the near lack of Variscan record of partial melting.

690 New zircon growth during anatexis is considered to exclusively result from the  
691 dissolution of pre-existing protolith zircon grains and re-precipitation of new grains (or  
692 overgrowths) from the melt phase (Kelsey et al., 2008; Mintrone et al., 2020; Watson,  
693 1996; Yakymchuk and Brown, 2014). Experimental studies have determined the  
694 solubility of Zr in silicate melts, which is positively correlated with temperature and also  
695 depends on melt composition (Boehnke et al., 2013; Watson and Harrison, 1983).  
696 Figures 15a and b depict the Zr solubility of orthogneiss-derived melts calculated based  
697 on the major-element compositions retrieved from thermodynamic modelling.  
698 Estimated values strongly depend on temperature but are independent of the bulk  
699 water content of the protolith (Fig. 15b). The Zr budget of the orthogneiss is almost  
700 entirely hosted in zircon, since the Zr concentration of the other mineral phases is

701 negligible (Bea et al., 2006). It is therefore possible to calculate the proportion of the  
702 orthogneiss zircon budget that has to be dissolved in order to saturate the melt phase  
703 (Fig. 15c, d). At low water content (Fig. 15c), a 20 vol.% melt fraction is only reached  
704 for temperatures >850 °C and dissolution of 50 wt.% of the protolith zircon budget is  
705 required to saturate the melt. In contrast, at high H<sub>2</sub>O contents, the same melt fraction  
706 is reached at much lower temperatures and is associated with very limited zircon  
707 dissolution. Considering values relevant to the Masméjean case, for a bulk H<sub>2</sub>O content  
708 of 1.5 wt.%, the migmatite contains 18 vol.% melt at c. 700°C which can be saturated  
709 by dissolution of as little as 7 wt.% of the orthogneiss zircon budget (Fig. 15d).

710 Additional constraints related to the low melting temperature may further hinder zircon  
711 dissolution and suggest that this value of 7 wt.% should be considered as a maximum.  
712 First, since biotite hosts substantial amounts of zircon grains in metamorphic rocks  
713 (Clemens, 2003), its stability during low temperature melting would prevent protolith  
714 zircon grains from physically interacting with the melt phase (Bea, 1996; Yakymchuk  
715 and Brown, 2014). Second, the kinetics of zircon dissolution are expected to be  
716 particularly sluggish at the range of melting temperatures inferred for the Masméjean  
717 migmatites because this process is controlled by Zr diffusion in the melt (Watson,  
718 1996). This author modelled the dissolution kinetics of zircon immersed in a granitic  
719 melt at 650–700°C (relevant to the Masméjean migmatites) for a period of 1 Ma and  
720 showed that for grains having radii of 90–120 µm (as for the Masméjean  
721 orthogneisses), resorption would only affect a maximum 20 µm-thick rim. This  
722 thickness would even be smaller if the Zr solubility calibration of Boehnke et al. (2013)  
723 is considered.

724 The combined effects of all the processes outlined above collectively point to limited  
725 zircon dissolution and hence new crystallization upon cooling. All processes relate to  
726 the low-T, water-fluxed melting conditions of the orthogneiss source and readily explain  
727 the scarcity of Variscan zircon grains or overgrowths in the Masméjean metatexites,  
728 leucosomes and “low-Ba” granites. The fact that Variscan zircon dates were obtained  
729 in the “high-Ba” granites (Fig. 10) is consistent with their inferred higher temperature  
730 of formation, favoring higher solubility and faster diffusion of Zr in the melt; and the  
731 release of biotite-occluded grains owing to biotite breakdown. The main implication of  
732 these results is the very scant zircon record (<2% of the dated grains) of a yet non-

733 negligible melting event (which produced as a whole 10–20 vol.% melt on the local  
734 scale).

735 In contrast with the zircon behavior documented in this study, Rubatto et al. (2009)  
736 report extensive new zircon crystallization in Alpine migmatites formed through water-  
737 fluxed melting at similar temperatures to those of the Masméjean antiform. We note  
738 that the migmatites studied by Rubatto et al. (2009) developed at the expense of K-  
739 feldspar-poor protoliths (amphibole-bearing metasediments, metatonalites) and that  
740 melt-producing reactions, even in the presence of water, most likely involved the  
741 breakdown of biotite forming peritectic hornblende (Berger et al., 2008). This suggests  
742 that the elusive zircon record of water-fluxed melting as observed in our dataset is a  
743 feature of peraluminous granitic protoliths.

## 744 **6. Conclusion**

745 Anatectic orthogneisses exposed in the core of the Masméjean antiform experienced  
746 water-fluxed melting at 310–300 Ma during the late-orogenic evolution of the Variscan  
747 belt. Anatexis took place at low temperature which produced leucogranitic melts with  
748 low Sr–Ba, REE and Zr contents. Those melts were collected within the partially molten  
749 domain (leucosomes, which retain a significant crystal load of source-inherited K-  
750 feldspar) or extracted to higher crustal levels. At the same time, partial melting of the  
751 orthogneisses at greater depths and higher temperature (~800°C) generated granitic  
752 melts showing elevated Sr–Ba, REE and Zr contents. The external water which fluxed  
753 melting of the orthogneisses most likely originated from H<sub>2</sub>O-rich dioritic or granitic  
754 magmas ponding in the middle crust. Zircon U-Pb dating overwhelmingly yielded the  
755 crystallization ages of the granite protolith of the orthogneiss source (c. 542 Ma),  
756 whereas Variscan zircon grains or overgrowths formed in response to the melting event  
757 represent <2% of the data. This lack of Variscan zircon is intimately tied to the low  
758 melting temperature which is shown to restrict the amount of zircon that can be  
759 dissolved in the melt phase (in terms of melt solubility; dissolution kinetics; and physical  
760 occlusion of zircon in restitic biotite). Our case study highlights that zircon has little  
761 potential to record the timing and duration of low-T, water-fluxed anatectic episodes in  
762 collisional orogens, especially those involving granitic (K-feldspar-rich) protoliths.

763

764 **Acknowledgements**

765 We warmly thank G. Stevens, A. T. Laurent, A. Villaros, V. Janoušek, J. Bascou, J.-M.  
766 Montel, A. Vezinet, C. Chelle-Michou, G. Nicoli and M. J. Mayne for enlightening  
767 discussions on crustal melting and granite petrogenesis. G. Stevens is also thanked  
768 for having provided access to the CAF at SUN. The help of A. Laurie during the SEM  
769 sessions was greatly appreciated. We also thank C. Guilbaud for making the thin  
770 sections. We are grateful to Xian-Hua Li for editorial handling and I. Williams and an  
771 anonymous reviewer for their thorough and constructive reviews. This work has been  
772 supported by CNRS/INSU grants to JFM and a travel grant from the UJM awarded to  
773 SC. This is IRP BuCoMO contribution A7.

774 **Figures and Tables captions**

775 Figure 1: (a) Sketch map showing exposed Variscan domains in Western Europe along  
776 with the main inferred suture zones (MZ: Moldanubian Zone, RHZ: Rheno-Hercynian  
777 Zone, STZ: Saxo-Thuringian Zone); (b) Geological map of the Eastern French Massif  
778 Central centered on the Velay dome, adapted from Chantraine et al. (1996).

779 Figure 2: Geological map at scale 1/80,000 of the Masméjean unit and selected cross-  
780 sections depicting the main lithotectonic features and the location of the dated  
781 samples. Drawn after our field survey and Briand et al. (1994); Lapadu-Hargues  
782 (1947); Négron (1979). The white stars outline available geochronological data on the  
783 emplacement and maximum depositional age of the orthogneiss (C'17: Couzinié et al.  
784 (2017)) and metasedimentary (C'19: Couzinié et al. (2019)) protoliths, respectively.

785 Figure 3: Representative photo(micro)graphs of migmatites from the core of the  
786 Masméjean antiform, developed at the expense of augen gneisses: (a) metatexite with  
787 segregated neosome in the form of leucocratic quartzofeldspathic layers (leucosome)  
788 and biotite-rich melanocratic layers; (b) syn-anatectic folding of the metatexites  
789 evidenced by the leucosome distribution within fold hinges, reflecting the collection of  
790 anatectic liquids in low-strain domains; (c and d) 10 to 20 cm thick leucosomes  
791 discordant with the anatectic foliation of metatexites; (e) paragneiss resister within  
792 augen gneiss-derived migmatites and rounded intrusion of K-rich diorite ("vaugnerite")  
793 intricately associated with coarse-grained Qz-feldspar domains; (f) contact between a  
794 Ms-Bt melanosome and a biotite-bearing granitic leucosome showing thin quartz films  
795 distributed along phase boundaries (cross-polarized light); (g) microstructure of a

796 biotite-bearing granitic leucosome with interstitial quartz locally showing cusped  
797 contacts with adjacent feldspar grains and well-equilibrated feldspar–feldspar triple  
798 junctions (cross-polarized light); (h) Bt–Sil leucosome (plane-polarized light).

799 Figure 4: The high-strain zone located at the interface between the anatectic domain  
800 and the unmelted cover in the southwestern flank of the Masméjean antiform  
801 (“Mylonitic Metamorphic Vellave Zone” of Bouilhol et al. (2006)): (a) intense folding in  
802 Bt–Sil paragneisses, with the axial plane parallel to the regional  $S_n$  foliation; (b) top-to-  
803 the NE  $C'$  shear bands within mylonitic augen gneisses; (c) granite sill injected within  
804 Bt–Sil paragneisses and subsequently affected by post-magmatic top-to-the S  
805 shearing at the brittle–ductile transition; (d) drag folds affecting Bt–Sil paragneisses  
806 and intrusive granite veins indicating that top-to-the NE shearing was coeval to granitic  
807 magmatism. The high-strain zone along the eastern flank of the antiform (Villefort  
808 Shear Zone): (e) steeply-dipping granite sills concordant within the foliation of Bt–Sil  
809 paragneisses; (f) quartzite layer showing a nearly vertical foliation and horizontal  
810 mineral lineation marked by scarce Bt aggregates; (g) magmatic layering in a  
811 decametric granite body evidenced by the accumulation of K-feldspar megacrysts; (h)  
812 polished rock slab of sample CHA-15-41 with a mm-scale shear band (arrow) showing  
813 marked grain-size reduction and subsequent alteration; (i) fractured K-feldspar  
814 phenocryst and sericitization of the plagioclase-rich matrix within the same sample  
815 (cross-polarized light).

816 Figure 5: Representative photo(micro)graphs of intrusive granites from the And–Bt–  
817 Crd zone in the Masméjean antiform: (a, b) post-tectonic pink leucogranite dykes  
818 cutting across the foliation of unmelted augen gneisses; (c) fine-grained porphyritic  
819 granite sill concordant within the foliation of paragneisses themselves embedded as a  
820 decametre-sized raft in augen gneisses; (d) texture of granite sample CHA-15-33  
821 showing the planar orientation of biotite and muscovite and the occurrence of mm-  
822 sized embayed quartz phenocrysts suggesting emplacement at shallow crustal levels  
823 (cross-polarized light); (e) polished slab of granite sample CHA-15-29 collected from a  
824 pink granite dyke.

825 Figure 6: Major element composition of the investigated metatexites, leucosomes and  
826 granites. (a) P–Q, (b) B–A, (c)  $K/(K+Na)$  vs. B and (d) B vs.  $Mg/(Fe+Mg)$  cationic  
827 classification diagrams of Debon and Le Fort (1988). The subdivisions of Villaseca et  
828 al. (1998) are indicated in plot (b) along with the experimental melt compositions

829 generated by high-temperature melting of a peraluminous orthogneiss . The grey field  
830 depicts the compositional range of local orthogneisses affiliated to the Velay  
831 Orthogneiss Formation. Data from Couzinié et al. (2017) and this study.

832 Figure 7: Rare Earth Elements patterns normalized to the chondrite values (Boynnton,  
833 1984) and spider diagrams for key trace element normalized to a representative augen  
834 gneiss composition (SC-14-33). The grey fields depict the compositional range of local  
835 augen gneisses (data from Couzinié et al. (2017)).

836 Figure 8: Representative cathodoluminescence images of zircon grains from  
837 metatexite, leucosome and granite samples of the Masméjean unit. The locations of  
838 laser spots are indicated along with the spot name (zXX). The letters a, b, c refer to  
839 the analytical session number (see Supplementary Text and Tables 2 to 5). The  
840 corresponding  $^{206}\text{Pb}/^{238}\text{U}$  dates are quoted with  $\pm 2\sigma$  uncertainty, in Ma. All displayed  
841 analyses are concordant at >95% (except those in italic).

842 Figure 9: Tera-Wasserburg diagrams ( $^{238}\text{U}/^{206}\text{Pb}$  vs.  $^{207}\text{Pb}/^{206}\text{Pb}$ ) for zircon grains from  
843 the orthogneiss, metatexites and leucosome samples. Error ellipses and dates are  
844 displayed at  $2\sigma$  level of uncertainty. Analyses were not corrected from common Pb.  
845 Yellow ellipses are those considered for Concordia date calculations.

846 Figure 10: Tera-Wasserburg diagrams ( $^{238}\text{U}/^{206}\text{Pb}$  vs.  $^{207}\text{Pb}/^{206}\text{Pb}$ ) for zircon grains  
847 from granite samples. Error ellipses and dates are displayed at  $2\sigma$  level of uncertainty.  
848 Analyses were not corrected from common Pb except those with dotted error ellipses.  
849 Yellow ellipses are those considered for Concordia date calculations.

850 Figure 11: Histogram showing the  $^{206}\text{Pb}/^{238}\text{U}$  dates measured on zircon grains from  
851 leucosomes and granites. Bin width is 15 Ma. Available zircon  $^{206}\text{Pb}/^{238}\text{U}$  dates  
852 (concordance: 95–105%) for the Velay Orthogneiss Formation (in red) and regional  
853 metasediments (in blue, N=107 and 445, respectively) are from Chelle-Michou et al.  
854 (2017), Couzinié et al. (2019); Couzinié et al. (2017) and this study, represented as  
855 Kernel Density Estimates. The latter were calculated using the DensityPlotter program  
856 of Vermeesch (2012) with a bandwidth set at 15 Ma.

857 Figure 12: (a, b) P–T and T– $X_{\text{H}_2\text{O}}$  pseudosections calculated using a representative  
858 orthogneiss composition (SC-14-33, from Couzinié et al. (2017)). White lines are melt  
859 modes (with numbers indicating melt vol.%). Initial water content of 0.53 wt.% for the

860 P–T pseudosection was adjusted to avoid subsolidus water saturation at 0.5 GPa.  
861 Mineral abbreviations after Whitney and Evans (2009). The white dots connected by  
862 black dashed lines refer to the location in the P–T– $X_{H_2O}$  space of the melts for which  
863 equilibrium Ba–Sr–Rb–Nb compositions have been computed. These calculations rely  
864 on the thermodynamically-constrained phase proportions and a set of partition  
865 coefficients for felsic systems compiled by Laurent et al. (2013) and listed in  
866 Supplementary Table S6. (c, d) Comparison of respective melt productivities (in vol.%)  
867 for representative orthogneiss and paragneiss samples (samples SC-14-33 and -41,  
868 respectively) at  $T < 800^\circ\text{C}$  and variable water contents (for a pressure of 0.5 GPa). The  
869 pseudosection for SC-14-41 (whole-rock composition available in Supplementary  
870 Table 1) was calculated using the same procedure and solution models as mentioned  
871 in section 3.3.

872 Figure 13: Petrogenesis of the Masméjean antiform leucosomes and granites.  
873 Comparison between leucosomes/granites and calculated melt compositions: (a)  
874 CIPW-normative ternary diagram; (b) Rb/Sr vs. Ba diagram; (c) Nb vs. Ba diagram.  
875 The Ba–Rb–Sr composition of K-feldspar from the local augen gneisses is from Négron  
876 (1979) while that of plagioclase is estimated from Bea et al. (1994).

877 Figure 14: Sketch cross-section across the southern Velay mid-crust (c. 10–15 km  
878 depth) at c. 305 Ma, right before the onset of doming. The Mylonitic Metamorphic  
879 Vellave Zone (MMVZ) corresponds to a high-strain shear zone developed at the  
880 interface between the anatectic and unmelted domains. Granite magmas formed at the  
881 expense of the orthogneisses were either emplaced within the MMVZ or extracted to  
882 higher crustal levels where they crop out as dykes. In the partially molten domain,  
883 water-fluxed melting possibly resulted from (i) diffusive transfer of magmatic  $H_2O$  along  
884 chemical potential gradients between orthogneisses and water-rich granitic melts  
885 ( $X_{H_2O} > 8$  wt.%) generated at pressures in excess of 1 GPa (>35 km depth, considering  
886 and average crustal density of  $2700 \text{ kg}\cdot\text{m}^{-3}$ , left part of the figure); (ii) the exsolution of  
887 magmatic water following the crystallization of high–K dioritic bodies (“vaugnerites”,  
888 right part of the figure).

889 Figure 15: (a) and (b): calculated maximal Zr concentration (in ppm) in the melt phase  
890 for a fully hydrated (at 0.5 GPa) orthogneiss composition (SC-14-33) in the P–T space  
891 and along a T– $X_{H_2O}$  section set at 0.5 GPa, based on the solubility equation of Boehnke  
892 et al. (2013). The Zr concentration of the stoichiometric zircon was set at 497644 ppm

893 and the average Zr content of the protolith at 115 ppm (average value for the local  
894 augen gneisses, data from Couzinié et al. (2017)). (c) and (d): calculated proportion  
895 (white lines, in wt.%) of the orthogneiss zircon budget to be dissolved in order to  
896 saturate the melt phase. Black dotted lines and bold numbers are melt modes in vol.%.

897 Table 1: Chemical composition of augen gneiss sample SC14-33 used in the modelling  
898 (in wt.% for major oxides, in ppm for trace elements). H<sub>2</sub>O content was adjusted to  
899 reach full hydration (but no water saturation) at the solidus for a pressure of 0.5 GPa.

900

901 Supplementary Figure SF1: CL image, location of laser spots and associated  
902 <sup>206</sup>Pb/<sup>238</sup>U dates (discordant if in italics) for orthogneisses CHA-15-52 and -35 and  
903 metatexites CHA-15-17 and -47. «ns» means that no reliable date was retrieved.

904 Supplementary Figure SF2: CL image, location of laser spots and associated  
905 <sup>206</sup>Pb/<sup>238</sup>U dates (discordant if in italics) for leucosome CHA-15-48 and metatexite  
906 CHA-15-65M. «ns» means that no reliable date was retrieved.

907 Supplementary Figure SF3: CL image, location of laser spots and associated  
908 <sup>206</sup>Pb/<sup>238</sup>U dates (discordant if in italics) for leucosomes CHA-15-63, 65L and -43. «ns»  
909 means that no reliable date was retrieved.

910 Supplementary Figure SF4: CL image, location of laser spots and associated  
911 <sup>206</sup>Pb/<sup>238</sup>U dates (discordant if in italics) for granites CHA-15-19, -24, -34 and -41. «ns»  
912 means that no reliable date was retrieved.

913 Supplementary Figure SF5: CL image, location of laser spots and associated  
914 <sup>206</sup>Pb/<sup>238</sup>U dates (discordant if in italics) for granites CHA-15-25, -33, -51, -49. «ns»  
915 means that no reliable date was retrieved.

916

917 Supplementary Table S1: Whole-rock major and trace element compositions obtained  
918 on the Masméjean antiform samples.

919 Supplementary Table S2: Results of LA-ICP-MS U–Pb analyses of zircon standards  
920 performed during the sessions at GUF, 2nd and 3rd of May, 2016

921 Supplementary Table S3: Results of LA-ICP-MS U–Pb analyses of zircon standards  
922 performed during the session at ETH Zürich, 12th of February, 2017

923 Supplementary Table S4: Results of LA-ICP-MS zircon U–Pb analyses performed  
924 during the sessions at GUF, 2nd and 3rd of May, 2016

925 Supplementary Table S5: Results of LA-ICP-MS zircon U–Pb analyses performed  
926 during the session at ETH Zürich, 12<sup>th</sup> of February, 2017

927 Supplementary Table S6: Set of partition coefficients for felsic systems (compiled by  
928 Laurent et al. (2013)).

929

## 930 **References**

931 Barbey, P., Villaros, A., Marignac, C., Montel, J.M., 2015. Multiphase melting, magma  
932 emplacement and P-T-time path in late-collisional context: the Velay example (Massif  
933 Central, France). *Bulletin de la Société Géologique de France* 186, 93-116.

934 Bea, F., 1996. Residence of REE, Y, Th and U in granites and crustal protoliths;  
935 implications for the chemistry of crustal melts. *Journal of Petrology* 37, 521-552.

936 Bea, F., Montero, P., Ortega, M., 2006. A LA-ICP-MS evaluation of Zr reservoirs in  
937 common crustal rocks: Implications for Zr and Hf geochemistry, and zircon-forming  
938 processes. *The Canadian Mineralogist* 44, 693-714.

939 Bea, F., Pereira, M.D., Stroh, A., 1994. Mineral/leucosome trace-element partitioning  
940 in a peraluminous migmatite (a laser ablation-ICP-MS study). *Chemical Geology* 117,  
941 291-312.

942 Berger, A., Burri, T., Alt-Epping, P., Engi, M., 2008. Tectonically controlled fluid flow  
943 and water-assisted melting in the middle crust: An example from the Central Alps.  
944 *Lithos* 102, 598-615.

945 Boehnke, P., Watson, E.B., Trail, D., Harrison, T.M., Schmitt, A.K., 2013. Zircon  
946 saturation re-revisited. *Chemical Geology* 351, 324-334.

947 Bouilhol, P., Leyreloup, A.F., Delor, C., Vauchez, A., Monié, P., 2006. Relationships  
948 between lower and upper crust tectonic during doming: the mylonitic southern edge

949 of the Velay metamorphic core complex (Cévennes-French Massif Central).  
950 *Geodinamica Acta* 19, 137-153.

951 Boynton, W.V., 1984. Cosmochemistry of the rare earth elements: meteorite studies,  
952 in: Henderson, P. (Ed.), *Rare Earth Element Geochemistry*. Elsevier, Amsterdam, pp.  
953 63-114.

954 Briand, B., Négron, J., Viard, M., Combémoré, R., Couturié, J.-P., 1994. Carte géol.  
955 France (1/50 000), feuille Le Bleymard (863). BRGM, Orléans.

956 Brouand, M., Banzet, G., Barbey, P., 1990. Zircon behaviour during crustal anatexis.  
957 Evidence from the Tibetan Slab migmatites (Nepal). *Journal of Volcanology and*  
958 *Geothermal Research* 44, 143-161.

959 Burg, J.-P., Vanderhaeghe, O., 1993. Structures and way-up criteria in migmatites,  
960 with application to the Velay dome (French massif Central). *Journal of Structural*  
961 *Geology* 15, 1293-1301.

962 Campbell, I.H., Reiners, P.W., Allen, C.M., Nicolescu, S., Upadhyay, R., 2005. He–  
963 Pb double dating of detrital zircons from the Ganges and Indus Rivers: Implication for  
964 quantifying sediment recycling and provenance studies. *Earth and Planetary Science*  
965 *Letters* 237, 402-432.

966 Castro, A., Patiño Douce, A.E., Corretgé, L.G., De la Rosa, J., El-Biad, M., El-Hmidi,  
967 H., 1999. Origin of peraluminous granites and granodiorites, Iberian massif, Spain: an  
968 experimental test of granite petrogenesis. *Contributions to Mineralogy and Petrology*  
969 135, 255-276.

970 Chantraine, J., Autran, A., Cavelier, C., 1996. Carte géologique de la France à  
971 l'échelle du millionième, 6ème édition. BRGM, Orléans.

972 Chelle-Michou, C., Laurent, O., Moyen, J.-F., Block, S., Paquette, J.-L., Couzinié, S.,  
973 Gardien, V., Vanderhaeghe, O., Villaros, A., Zeh, A., 2017. Pre-Cadomian to late-  
974 Variscan odyssey of the eastern Massif Central, France: Formation of the West  
975 European crust in a nutshell. *Gondwana Research* 46, 170-190.

976 Clemens, J., 2003. S-type granitic magmas—petrogenetic issues, models and  
977 evidence. *Earth-Science Reviews* 61, 1-18.

978 Clemens, J.D., Vielzeuf, D., 1987. Constraints on melting and magma production in  
979 the crust. *Earth and Planetary Science Letters* 86, 287-306.

980 Connolly, J.A.D., 2009. The geodynamic equation of state: What and how.  
981 *Geochemistry, Geophysics, Geosystems* 10, 1-19.

982 Costa, S., Rey, P., 1995. Lower crustal rejuvenation and growth during post-  
983 thickening collapse: insights from a crustal cross section through a Variscan  
984 metamorphic core complex. *Geology* 23, 905-908.

985 Couzinié, S., 2017. Evolution of the continental crust and significance of the zircon  
986 record, a case study from the French Massif Central. *Saint-Etienne - Stellenbosch*, p.  
987 431.

988 Couzinié, S., Laurent, O., Chelle-Michou, C., Bouilhol, P., Paquette, J.L., Gannoun,  
989 A.-M., Moyen, J.F., 2019. Detrital zircon U–Pb–Hf systematics of Ediacaran  
990 metasediments from the French Massif Central: Consequences for the crustal  
991 evolution of the north Gondwana margin. *Precambrian Research* 324, 269–284.

992 Couzinié, S., Laurent, O., Moyen, J.F., Zeh, A., Bouilhol, P., Villaros, A., 2016. Post-  
993 collisional magmatism: Crustal growth not identified by zircon Hf-O isotopes. *Earth  
994 and Planetary Science Letters* 456, 182-195.

995 Couzinié, S., Laurent, O., Poujol, M., Mintrone, M., Chelle-Michou, C., Moyen, J.-F.,  
996 Bouilhol, P., Vezinet, A., Marko, L., 2017. Cadomian S-type granites as basement  
997 rocks of the Variscan belt (Massif Central, France): Implications for the crustal  
998 evolution of the north Gondwana margin. *Lithos* 286-287, 16-34.

999 Couzinié, S., Moyen, J.F., Villaros, A., Paquette, J.L., Scarrow, J.H., Marignac, C.,  
1000 2014. Temporal relationships between Mg-K mafic magmatism and catastrophic  
1001 melting of the Variscan crust in the southern part of Velay Complex (Massif Central,  
1002 France). *Journal of GEOsciences*, 69-86.

1003 Debon, F., Le Fort, P., 1988. A cationic classification of common plutonic rocks and  
1004 their magmatic associations: principles, method, applications. *Bull. Minéral.* 111, 493-  
1005 511.

1006 Deroin, J.-P., Prost, A.E., 1993. Déformation tardi-hercynienne du batholite de  
1007 Villefort (Mont Lozère et Massif de la Borne). *Ses rapports avec les sédiments*

1008 permiens du Pont-de-Montvert (Cévennes, Sud-Est du Massif central). *Géologie de*  
1009 *la France* 2, 23-30.

1010 Didier, A., Bosse, V., Boulvais, P., Bouloton, J., Paquette, J.L., Montel, J.M., Devidal,  
1011 J.L., 2013. Disturbance versus preservation of U–Th–Pb ages in monazite during  
1012 fluid–rock interaction: textural, chemical and isotopic in situ study in microgranites  
1013 (Velay Dome, France). *Contributions to Mineralogy and Petrology* 165, 1051-1072.

1014 Dusséaux, C., Gébelin, A., Boulvais, P., Gardien, V., Grimes, S., Mulch, A., 2019.  
1015 Meteoric fluid-rock interaction in Variscan shear zones. *Terra Nova* 31, 366-372.

1016 Faure, M., Lardeaux, J.-M., Ledru, P., 2009. A review of the pre-Permian geology of  
1017 the Variscan French Massif Central. *Comptes Rendus Geoscience* 341, 202-213.

1018 García-Arias, M., Corretgé, L.G., Castro, A., 2012. Trace element behavior during  
1019 partial melting of Iberian orthogneisses: An experimental study. *Chemical Geology*  
1020 292-293, 1-17.

1021 Guergouz, C., Martin, L., Vanderhaeghe, O., Thébaud, N., Fiorentini, M., 2018.  
1022 Zircon and monazite petrochronologic record of prolonged amphibolite to granulite  
1023 facies metamorphism in the Ivrea-Verbano and Strona-Ceneri Zones, NW Italy.  
1024 *Lithos* 308-309, 1-18.

1025 Harley, S.L., 2016. A matter of time: The importance of the duration of UHT  
1026 metamorphism. *Journal of Mineralogical and Petrological Sciences* 111, 50-72.

1027 Harris, N., Vance, D., Ayres, M., 2000. From sediment to granite: timescales of  
1028 anatexis in the upper crust. *Chemical Geology* 162, 155-167.

1029 Holland, T.J.B., Powell, R., 1998. An internally consistent thermodynamic data set for  
1030 phases of petrological interest. *Journal of Metamorphic Geology* 16, 309-343.

1031 Janoušek, V., Farrow, C.M., Erban, V., 2006. Interpretation of Whole-rock  
1032 Geochemical Data in Igneous Geochemistry: Introducing Geochemical Data Toolkit  
1033 (GCDkit). *Journal of Petrology* 47, 1255-1259.

1034 Janoušek, V., Moyen, J.F., 2019. Whole-rock geochemical modelling of granite  
1035 genesis – the current state of play. Geological Society, London, Special Publications  
1036 491, 267-291.

1037 Johannes, W., 1983. On the origin of layered migmatites, in: Atherton, M.P., Gribble,  
1038 C.D. (Eds.), *Migmatites, Melting, and Metamorphism*.

1039 Johannes, W., Holtz, F., 1996. *Petrogenesis and experimental petrology of granitic*  
1040 *rocks*. Springer, Berlin Heidelberg New York.

1041 Kelsey, D.E., Clark, C., Hand, M., 2008. Thermobarometric modelling of zircon and  
1042 monazite growth in melt-bearing systems: examples using model metapelitic and  
1043 metapsammitic granulites. *Journal of Metamorphic Geology* 26, 199-212.

1044 Korhonen, F.J., Clark, C., Brown, M., Bhattacharya, S., Taylor, R., 2013. How long-  
1045 lived is ultrahigh temperature (UHT) metamorphism? Constraints from zircon and  
1046 monazite geochronology in the Eastern Ghats orogenic belt, India. *Precambrian*  
1047 *Research* 234, 322-350.

1048 Lapadu-Hargues, P., 1947. Les massifs de la Margeride et du mont Lozère et leurs  
1049 bordures. *Bull. Serv. Carte géol Fr.* 46, 420-432.

1050 Laurent, A.T., Bingen, B., Duchene, S., Whitehouse, M.J., Seydoux-Guillaume, A.-m.,  
1051 Bosse, V., 2018. Decoding a protracted zircon geochronological record in ultrahigh  
1052 temperature granulite, and persistence of partial melting in the crust, Rogaland,  
1053 Norway. *Contributions to Mineralogy and Petrology* 173.

1054 Laurent, O., Couzinié, S., Zeh, A., Vanderhaeghe, O., Moyen, J.-F., Villaros, A.,  
1055 Gardien, V., Chelle-Michou, C., 2017. Protracted, coeval crust and mantle melting  
1056 during Variscan late-orogenic evolution: U–Pb dating in the eastern French Massif  
1057 Central. *International Journal of Earth Sciences* 106, 421-451.

1058 Laurent, O., Doucelance, R., Martin, H., Moyen, J.-F., 2013. Differentiation of the  
1059 late-Archaean sanukitoid series and some implications for crustal growth: Insights  
1060 from geochemical modelling on the Bulai pluton, Central Limpopo Belt, South Africa.  
1061 *Precambrian Research* 227, 186-203.

1062 Ledru, P., Courrioux, G., Dallain, C., Lardeaux, J.M., Montel, J.M., Vanderhaeghe,  
1063 O., Vitel, G., 2001. The Velay dome (French Massif Central): melt generation and  
1064 granite emplacement during orogenic evolution. *Tectonophysics* 342, 207-237.

1065 Lemirre, B., Cochelin, B., Duchene, S., de Saint Blanquat, M., Poujol, M., 2019.  
1066 *Origin and duration of late orogenic magmatism in the foreland of the Variscan belt*

1067 (Lesponne — Chiroulet — Neouvielle area, French Pyrenees). *Lithos* 336-337, 183-  
1068 201.

1069 Matte, P., 1991. Accretionary history and crustal evolution of the Variscan belt in  
1070 Western Europe. *Tectonophysics* 196, 309-337.

1071 Mezger, K., Krogstad, E.J., 1997. Interpretation of discordant U-Pb zircon ages: An  
1072 evaluation. *Journal of Metamorphic Geology* 15, 127-140.

1073 Mintrone, M., Galli, A., Laurent, O., Chelle-Michou, C., Schmidt, M.W., 2020.  
1074 Quantifying frozen melt in crustal rocks: A new melt-o-meter based on zircon rim  
1075 volumes. *Chemical Geology* 551.

1076 Montel, J.M., 1993. A model for monazite/melt equilibrium and application to the  
1077 generation of granitic magmas. *Chemical Geology* 110, 127-146.

1078 Montel, J.M., Marignac, C., Barbey, P., Pichavant, M., 1992. Thermobarometry and  
1079 granite genesis: the Hercynian low-P, high-T Velay anatectic dome (French Massif  
1080 Central). *Journal of Metamorphic Geology* 10, 1-15.

1081 Montel, J.M., Weisbrod, A., 1986. Characteristics and evolution of "vaugneritic  
1082 magmas": an analytical and experimental approach, on the example of the Cévennes  
1083 Médiannes (French Massif Central). *Bull. Minéral.* 109, 575-587.

1084 Moyen, J.F., Laurent, O., Chelle-Michou, C., Couzinié, S., Vanderhaeghe, O., Zeh,  
1085 A., Villaros, A., Gardien, V., 2017. Collision vs. subduction-related magmatism: Two  
1086 contrasting ways of granite formation and implications for crustal growth. *Lithos* 277,  
1087 154-177.

1088 Nasdala, L., Pidgeon, R.T., Wolf, D., Irmer, G., 1998. Metamictization and U-Pb  
1089 isotopic discordance in single zircons: a combined Raman microprobe and SHRIMP  
1090 ion probe study. *Mineralogy and Petrology* 62, 1-27.

1091 Négron, J., 1979. *Pétrologie et géochimie des formations quartzofeldspathiques de la*  
1092 *série mésozonale du Chassezac (Lozère, Massif Central français)*. Lyon, p. 175.

1093 O'Brien, T.M., Miller, E.L., 2014. Continuous zircon growth during long-lived granulite  
1094 facies metamorphism: a microtextural, U–Pb, Lu–Hf and trace element study of  
1095 Caledonian rocks from the Arctic. *Contributions to Mineralogy and Petrology* 168.

1096 Oliver, N.H.S., Bodorkos, S., Nemchin, A.A., Kinny, P.D., Watt, G.R., 1999.  
1097 Relationships between zircon U-Pb SHRIMP ages and leucosome type in migmatites  
1098 of the Halls Creek Orogen, Western Australia. *Journal of Petrology* 40, 1553-1575.

1099 Parat, F., Holtz, F., René, M., Almeev, R., 2009. Experimental constraints on  
1100 ultrapotassic magmatism from the Bohemian Massif (durbachite series, Czech  
1101 Republic). *Contributions to Mineralogy and Petrology* 159, 331-347.

1102 Patiño Douce, A.E., Harris, N., 1998. Experimental constraints on Himalayan  
1103 anatexis. *Journal of Petrology* 39, 690-710.

1104 Petford, N., Cruden, A.R., McCaffrey, K.J.W., Vigneresse, J.L., 2000. Granite magma  
1105 formation, transport and emplacement in the Earth's crust. *Nature* 408, 669-673.

1106 Rey, P.F., Teyssier, C., Whitney, D.L., 2009. The role of partial melting and  
1107 extensional strain rates in the development of metamorphic core complexes.  
1108 *Tectonophysics* 477, 135-144.

1109 Rosenberg, C.L., Handy, M.R., 2005. Experimental deformation of partially melted  
1110 granite revisited: implications for the continental crust. *Journal of Metamorphic  
1111 Geology* 23, 19-28.

1112 Rubatto, D., Chakraborty, S., Dasgupta, S., 2013. Timescales of crustal melting in  
1113 the Higher Himalayan Crystallines (Sikkim, Eastern Himalaya) inferred from trace  
1114 element-constrained monazite and zircon chronology. *Contributions to Mineralogy  
1115 and Petrology* 165, 349-372.

1116 Rubatto, D., Hermann, J., Berger, A., Engi, M., 2009. Protracted fluid-induced melting  
1117 during Barrovian metamorphism in the Central Alps. *Contributions to Mineralogy and  
1118 Petrology* 158, 703-722.

1119 Sawyer, E.W., 2010. Migmatites formed by water-fluxed partial melting of a  
1120 leucogranodiorite protolith: Microstructures in the residual rocks and source of the  
1121 fluid. *Lithos* 116, 273-286.

1122 Tafur, L.A., Diener, J.F.A., 2020. Mineral equilibrium constraints on the feasibility of  
1123 diffusive H<sub>2</sub>O-fluxed melting in the continental crust. *Journal of Metamorphic Geology*  
1124 38, 719-742.

1125 Taylor, R.J.M., Clark, C., Johnson, T.E., Harrison, R.J., 2019. Persistence of melt-  
1126 bearing Archean lower crust for >200 m.y.—An example from the Lewisian  
1127 Complex, northwest Scotland. *Geology* 48, 221-225.

1128 Vanderhaeghe, O., Laurent, O., Gardien, V., Moyen, J.F., G belin, A., Chelle-  
1129 Michou, C., Couzini , S., Villaros, A., Bellanger, M., 2020. Flow of partially molten  
1130 crust controlling construction, growth and collapse of the Variscan orogenic belt: the  
1131 geologic record of the French Massif Central. *BSGF - Earth Sciences Bulletin* 191.

1132 Vanderhaeghe, O., Teyssier, C., 2001. Partial melting and flow of orogens.  
1133 *Tectonophysics* 342, 451-472.

1134 Vermeesch, P., 2012. On the visualisation of detrital age distributions. *Chemical*  
1135 *Geology* 312-313, 190-194.

1136 Vigneresse, J.L., Barbey, P., Cuney, M., 1996. Rheological transitions during partial  
1137 melting and crystallization with application to felsic magma segregation and transfer.  
1138 *Journal of Petrology* 37, 1579-1600.

1139 Villaros, A., Laurent, O., Couzini , S., Moyen, J.F., Mintrone, M., 2018. Plutons and  
1140 domes: the consequences of anatectic magma extraction—example from the  
1141 southeastern French Massif Central. *International Journal of Earth Sciences* 107,  
1142 2819-2842.

1143 Villaseca, C., Barbero, L., Herreros, V., 1998. A re-examination of the typology of  
1144 peraluminous granite types in intracontinental orogenic belts. *Transactions of the*  
1145 *Royal Society of Edinburgh* 89, 113-119.

1146 Watson, E.B., 1996. Dissolution, growth and survival of zircons during crustal fusion:  
1147 kinetic principals, geological models and implications for isotopic inheritance.  
1148 *Transactions of the Royal Society of Edinburgh* 87, 43-56.

1149 Watson, E.B., Cherniak, D.J., Hanchar, J.M., Harrison, T.M., Wark, D.A., 1997. The  
1150 incorporation of Pb into zircon. *Chemical Geology* 141, 19-31.

1151 Watson, E.B., Harrison, T.M., 1983. Zircon saturation revisited: temperature and  
1152 composition effects in a variety of crustal magma types. *Earth and Planetary Science*  
1153 *Letters* 64, 295-304.

- 1154 Weinberg, R.F., Hasalová, P., 2015. Water-fluxed melting of the continental crust: A  
1155 review. *Lithos* 212-215, 158-188.
- 1156 Whitney, D.L., Evans, B.W., 2009. Abbreviations for names of rock-forming minerals.  
1157 *American Mineralogist* 95, 185-187.
- 1158 Wickham, S.M., Taylor, H.P.J., 1985. Stable isotopic evidence for large-scale  
1159 seawater infiltration in a regional metamorphic terrane; the Trois Seigneurs Massif,  
1160 Pyrenees, France. *Contributions to Mineralogy and Petrology* 91, 122-137.
- 1161 Yakymchuk, C., Brown, M., 2014. Behaviour of zircon and monazite during crustal  
1162 melting. *Journal of the Geological Society* 171, 465-479.

**Table 1:** Chemical composition of augen gneiss sample SC14-33 used in the modelling (in wt.% for major oxides, in ppm for trace elements). H<sub>2</sub>O content was adjusted to reach full hydration (but no water saturation) at the solidus for a pressure of 0.5 GPa.

SiO <sub>2</sub>	Al <sub>2</sub> O <sub>3</sub>	FeO	CaO	MgO	Na <sub>2</sub> O	K <sub>2</sub> O	TiO <sub>2</sub>	H <sub>2</sub> O	Ba	Nb	Rb	Sr
72.56	14.90	2.02	0.76	0.40	3.12	5.52	0.19	0.53	576	8	184	87

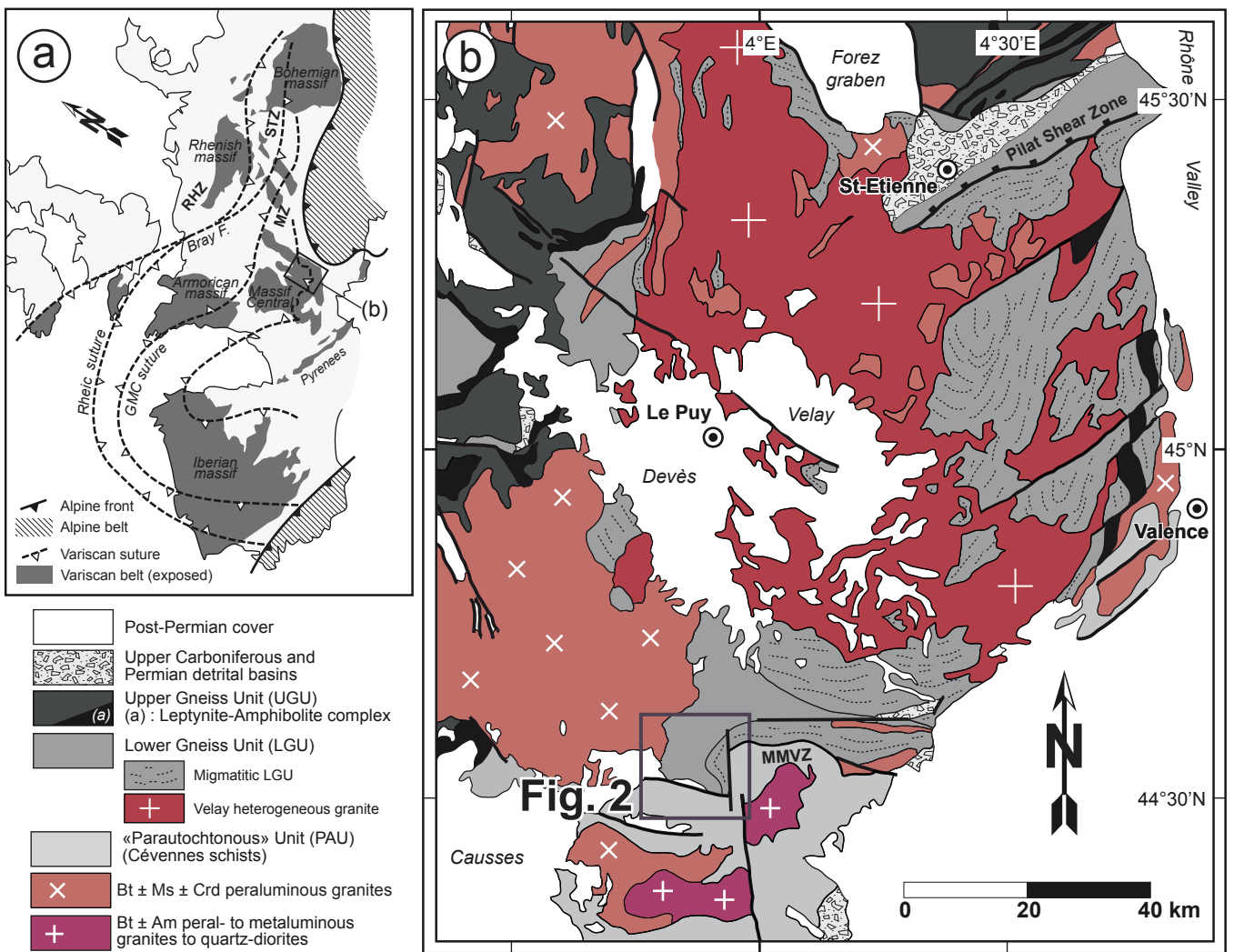


Figure 1: (a) Sketch map showing the repartition of exposed Variscan domains in Western Europe along with the main inferred suture zones (MZ: Moldanubian Zone, RHZ: Rheno-Hercynian Zone, STZ: Saxo-Thuringian Zone); (b) Geological map of the Eastern French Massif Central centered on the Velay dome, adapted from Chantraine et al. (1996).

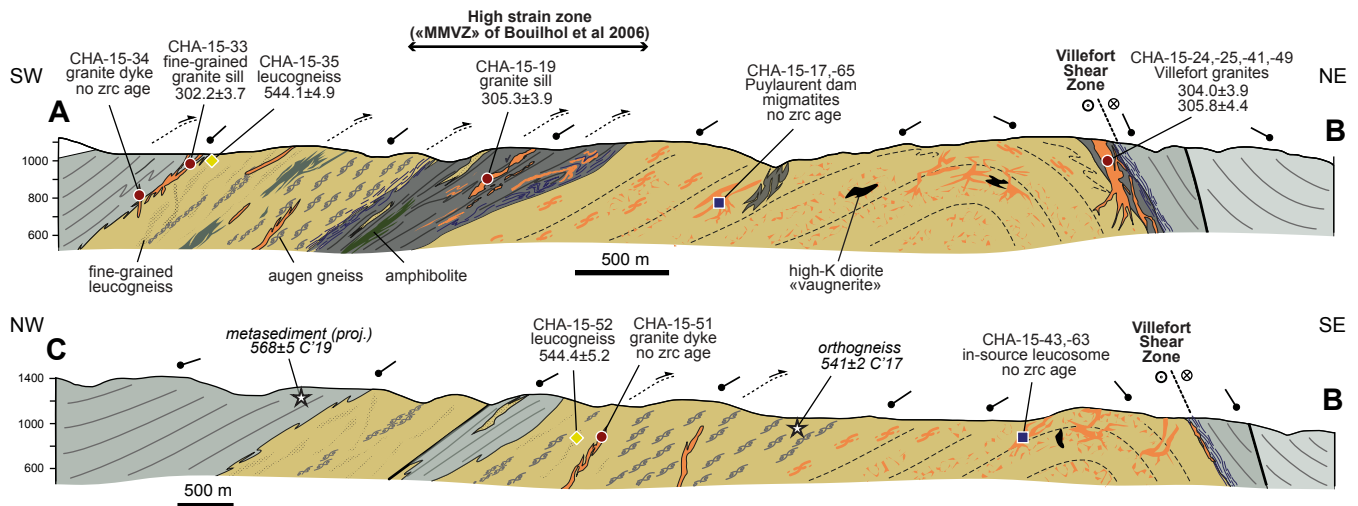
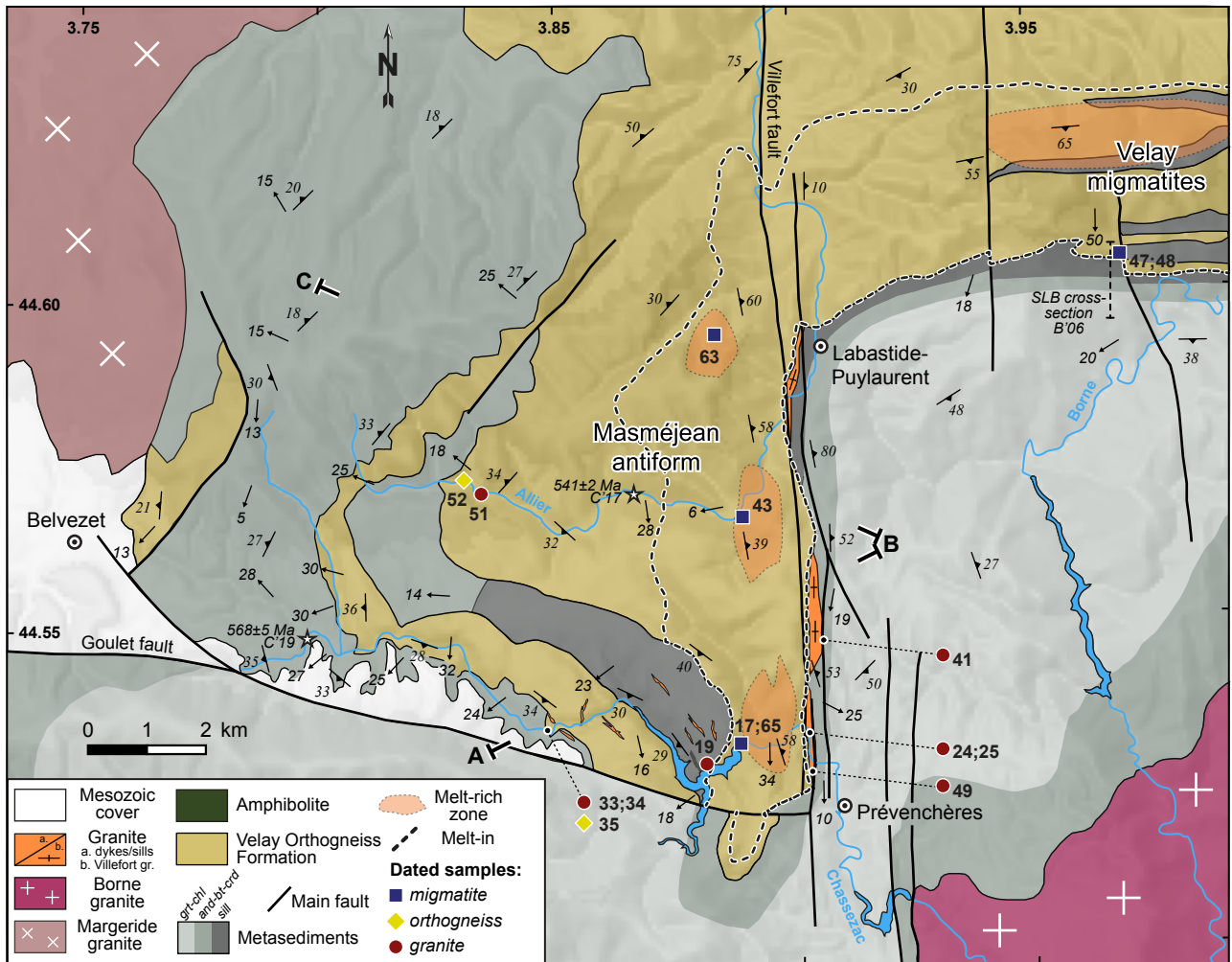


Figure 2: Geological map at scale 1/80,000 of the Masméjean unit and selected cross-sections depicting the main lithotectonic features and the location of the dated samples. Drawn after our field survey and the works of Briand et al. (1994); Lapaduhargues (1947); Négron (1979). The white stars outline available geochronological data on the emplacement and maximum depositional age of the orthogneiss (C'17: Couzinié et al. (2017)) and metasedimentary (C'19: Couzinié et al. (2019)) protoliths, respectively.

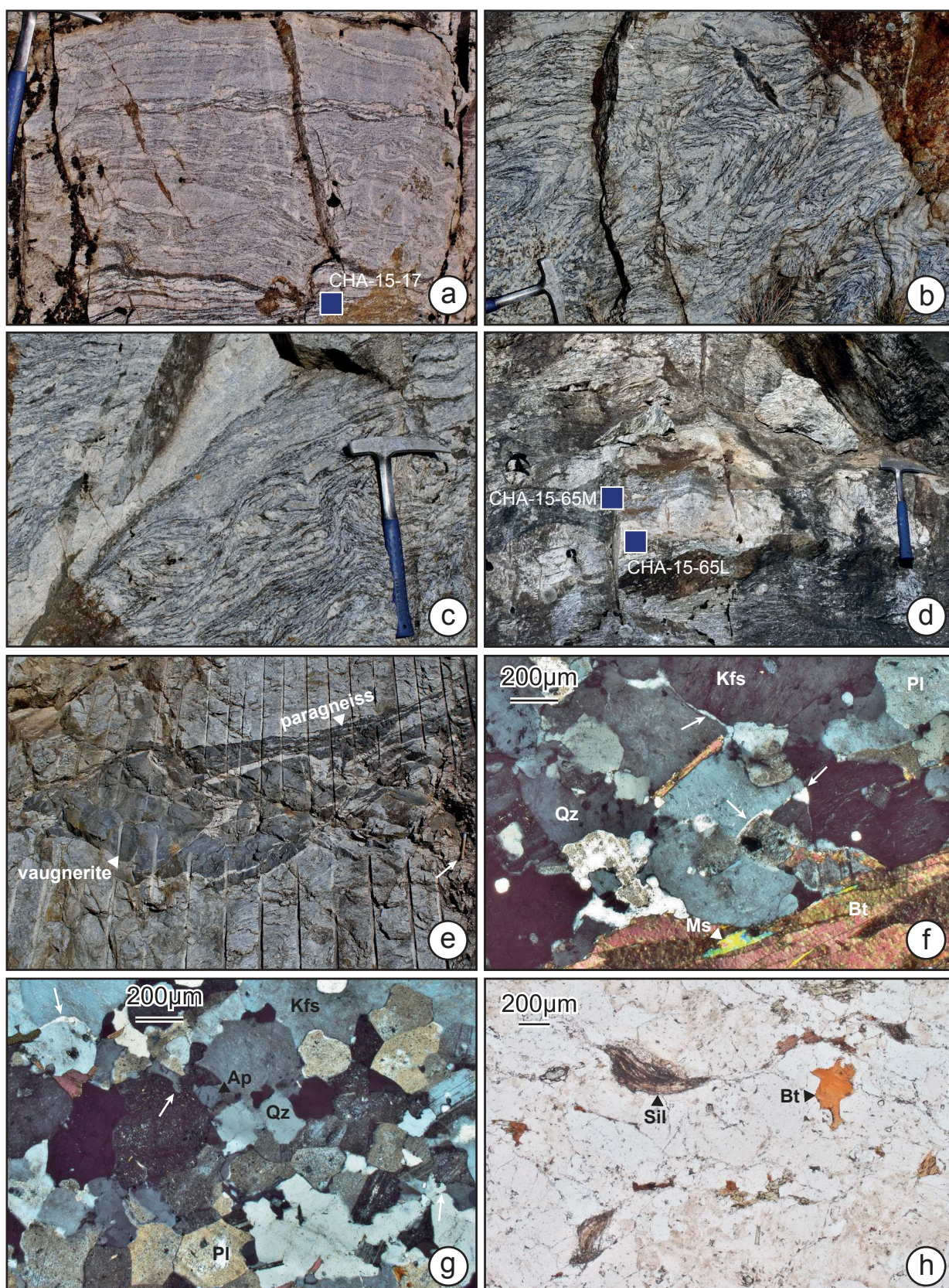


Figure 3: Representative photo(micro)graphs of migmatites from the core of the Masméjean antiform, developed at the expense of augen gneisses: (a) metatexite with segregated neosome in the form of leucocratic quartzofeldspathic layers (leucosome), locally folded, and biotite-rich melanocratic layers; (b) syn-anatectic folding of the metatexites evidenced by the leucosome distribution within fold hinges, reflecting the collection of anatectic liquids in low-strain domains; (c and d) 10 to 20 cm thick leucosomes discordant with the anatectic foliation of metatexites; (e) paragneiss resister within augen gneiss-derived migmatites and rounded intrusion of K-rich diorite ("vaugnerite") intricately associated with coarse-grained Qz-feldspar domains; (f) contact between a muscovite-biotite melanosome and a biotite-bearing granitic leucosome showing thin quartz films distributed along phase boundaries (cross-polarized light); (g) microstructure of a biotite-bearing granitic leucosome with interstitial quartz locally showing cusped contacts with adjacent feldspar grains and well-equilibrated feldspar-feldspar triple junctions (cross-polarized light); (h) biotite- and sillimanite-bearing leucosome (plane-polarized light).

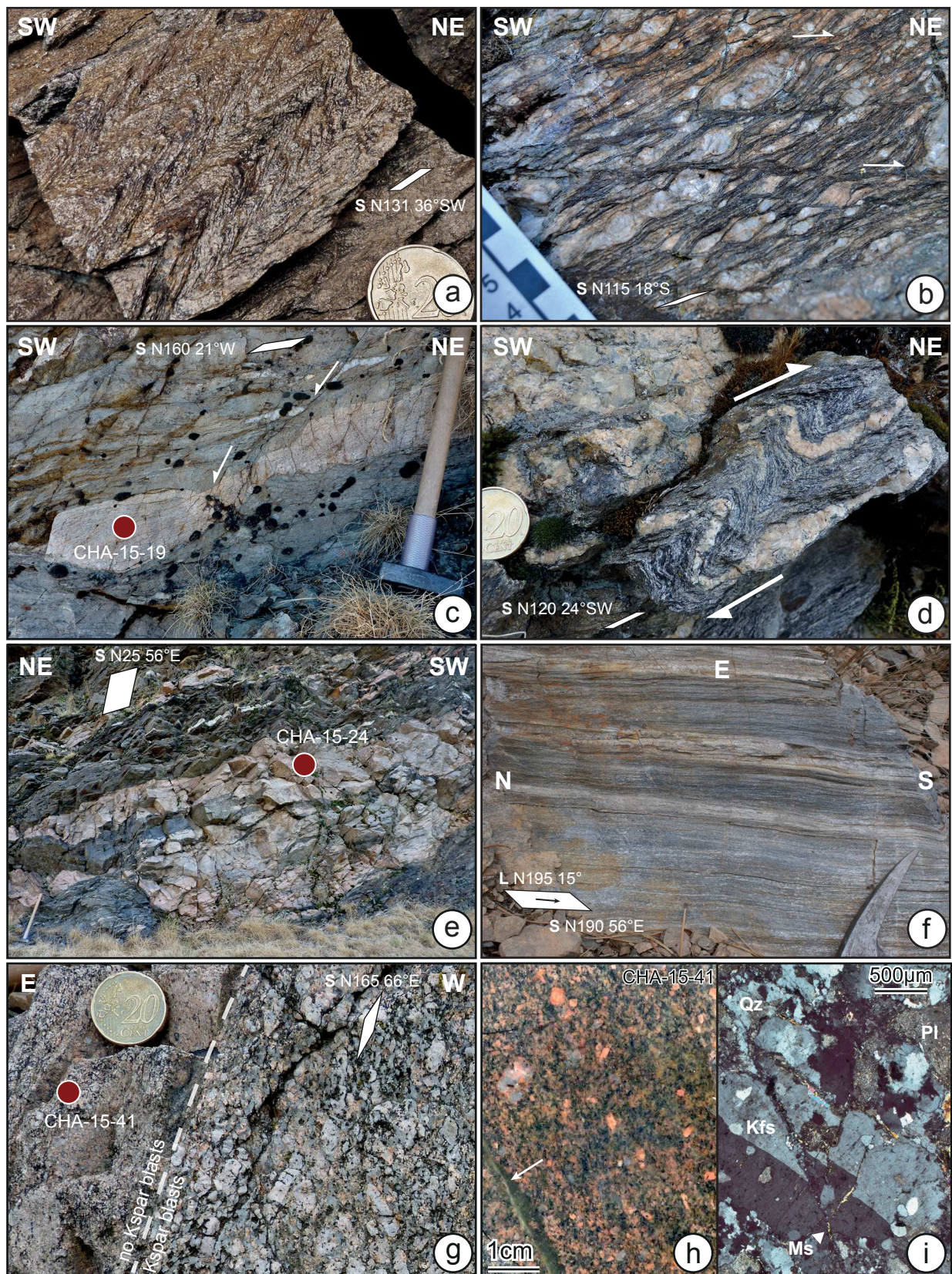


Figure 4: The high-strain zone located at the interface between the anatexitic domain and the unmolten cover in the southwestern flank of the Masméjean antiform (“Mylonitic Metamorphic Vellave Zone” of Bouilhol et al. (2006)): (a) intense folding in Bt–Sil-bearing paragneisses, with the axial plane parallel to the regional  $S_n$  foliation; (b) top-to-the NE  $C'$  shear bands within mylonitic augen gneisses; (c) granite sill injected within Bt–Sil-bearing paragneisses and subsequently affected by post-magmatic top-to-the S shearing at the brittle–ductile transition; (d) drag folds affecting Bt–Sil-bearing paragneisses and intrusive granite veins indicating that top-to-the NE shearing was coeval to granitic magmatism. The high-strain zone along the eastern flank of the antiform (Villefort Shear Zone): (e) steeply-dipping granite sills concordant within the foliation of Bt–Sil-bearing paragneisses; (f) quartzite layer showing a nearly vertical foliation and horizontal mineral lineation marked by scarce Bt aggregates; (g) magmatic layering in a decametric granite body evidenced by the accumulation of K-feldspar megacrysts; (h) polished rock slab of sample CHA-15-41 with a millimeter-scale shear band (arrow) showing marked grain-size reduction and subsequent alteration; (i) fractured K-feldspar phenocryst and sericitization of the plagioclase-rich matrix within the same sample (cross-polarized light).

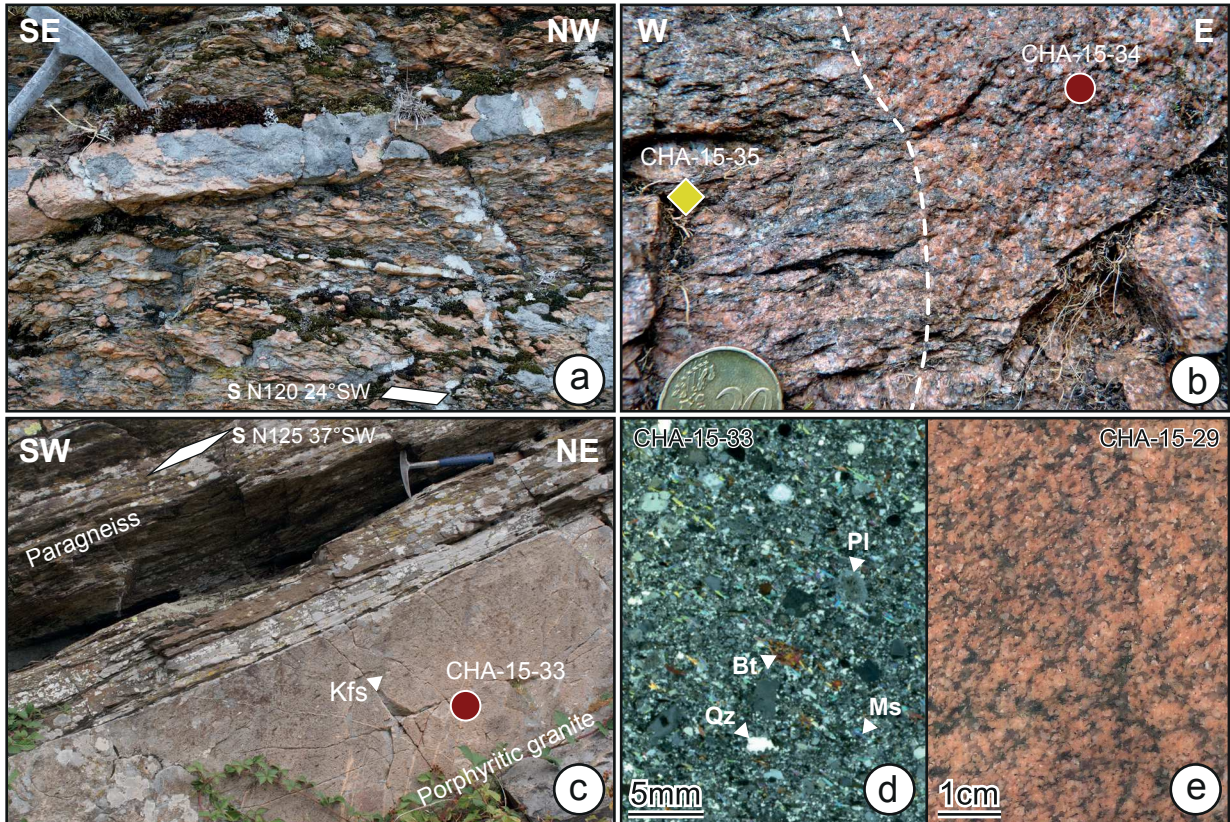


Figure 5: Representative photo(micro)graphs of intrusive granites from the And–Bt–Crd zone in the Masméjean antiform: (a, b) post-tectonic “pink” leucogranite dykes cutting across the foliation of unmolten augen gneisses; (c) fine-grained porphyritic granite sill concordant within the foliation of paragneisses themselves embedded as a decametric raft in augen gneisses; (d) texture of granite sample CHA-15-33 showing the planar orientation of biotite and muscovite and the occurrence of millimetric embayed quartz phenocrysts suggesting emplacement at shallow crustal levels (cross-polarized light); (e) polished slab of granite sample CHA-15-29 collected from a pink granite dyke.

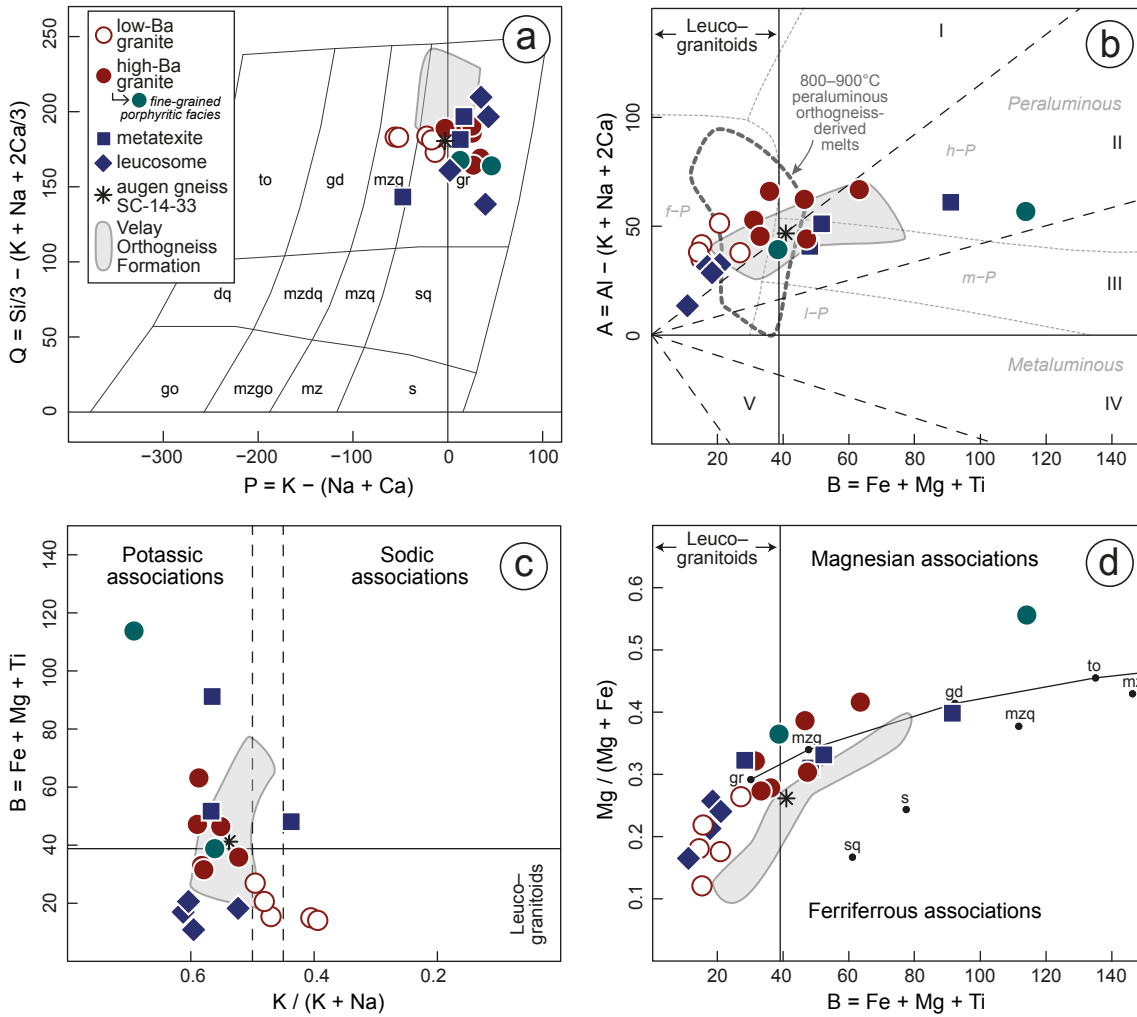


Figure 6: Major element composition of the investigated metatexites, leucosomes and granites from the Masméjean unit. (a) P–Q, (b) B–A, (c) K/(K+Na) vs. B and (d) B vs. Mg/(Fe+Mg) cationic classification diagrams of Debon and Le Fort (1988). The subdivisions of Villaseca et al. (1998) are indicated in plot (b) along with the experimental melt compositions generated by high-temperature melting of a peraluminous orthogneiss (García-Arias et al., 2012). The grey field depicts the compositional range of local orthogneisses affiliated to the Velay Orthogneiss Formation. Data from Couzinié et al. (2017) and this study.

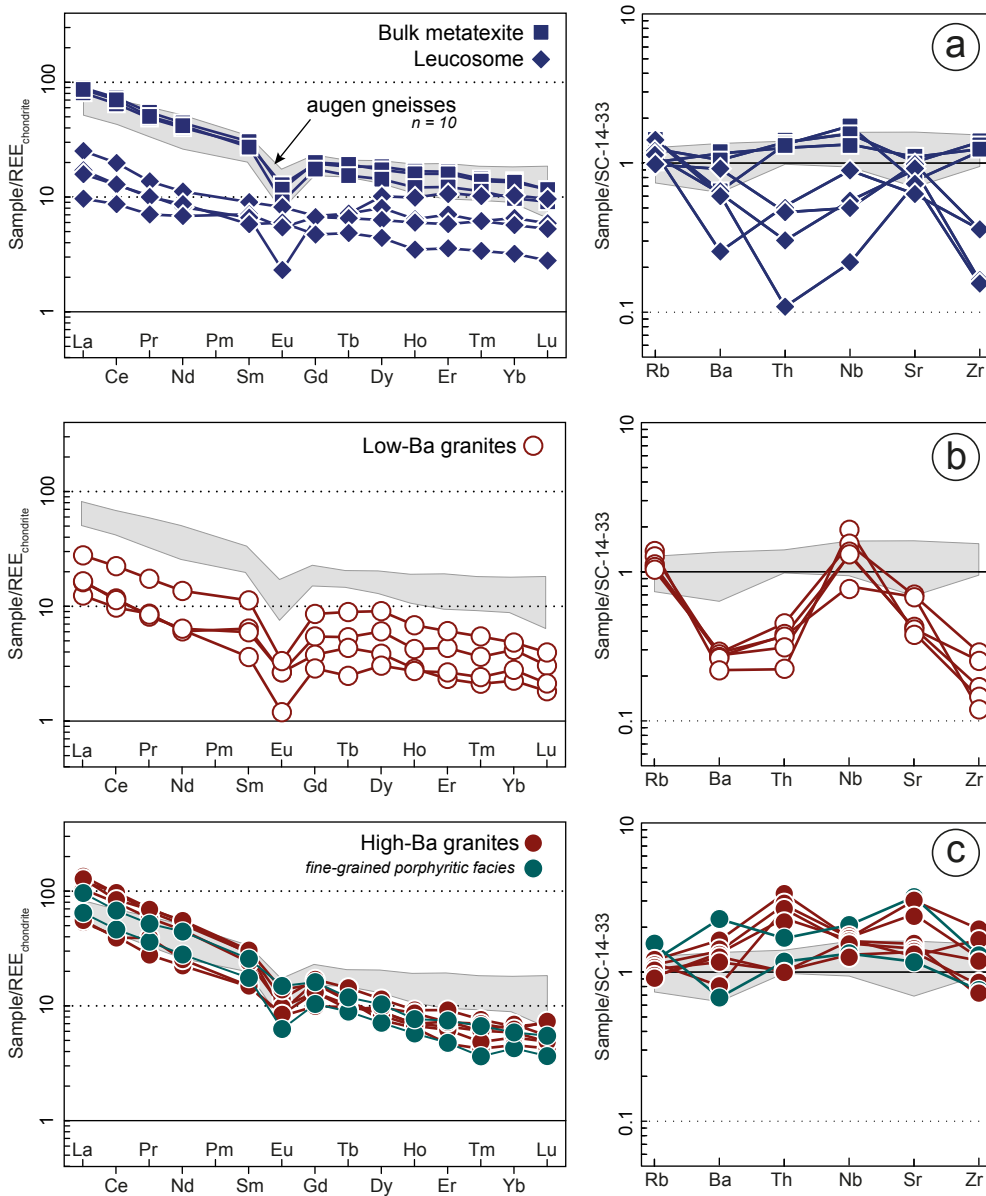


Figure 7: Rare Earth Elements patterns normalized to the chondrite values (Boynton, 1984) and spider diagrams for key trace element normalized to a representative augen gneiss composition (SC-14-33). The grey fields depicts the compositional range of local augen gneisses (data from Couzinié et al. (2017)).

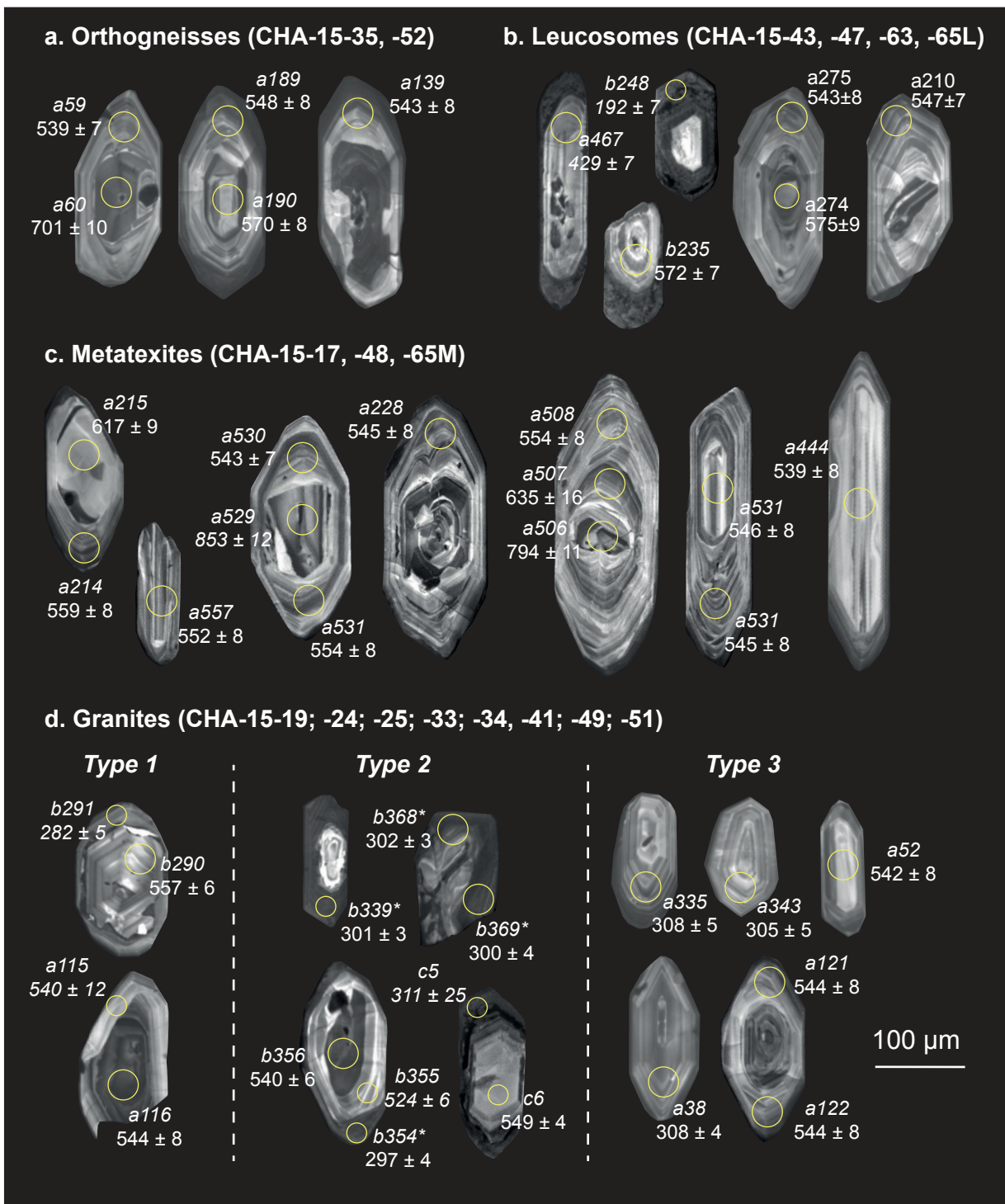


Figure 8: Representative cathodoluminescence images of zircon grains from metatexite, leucosome and granite samples of the Masméjean unit. The locations of laser spots are indicated along with the spot name (zXX). The letters a, b, c refer to the analytical session number (see Supplementary Text and Table). The corresponding  $^{206}\text{Pb}/^{238}\text{U}$  dates are quoted with  $\pm 2\sigma$  uncertainty, in Ma. All displayed analyses are concordant at  $>95\%$  (except those in italic).

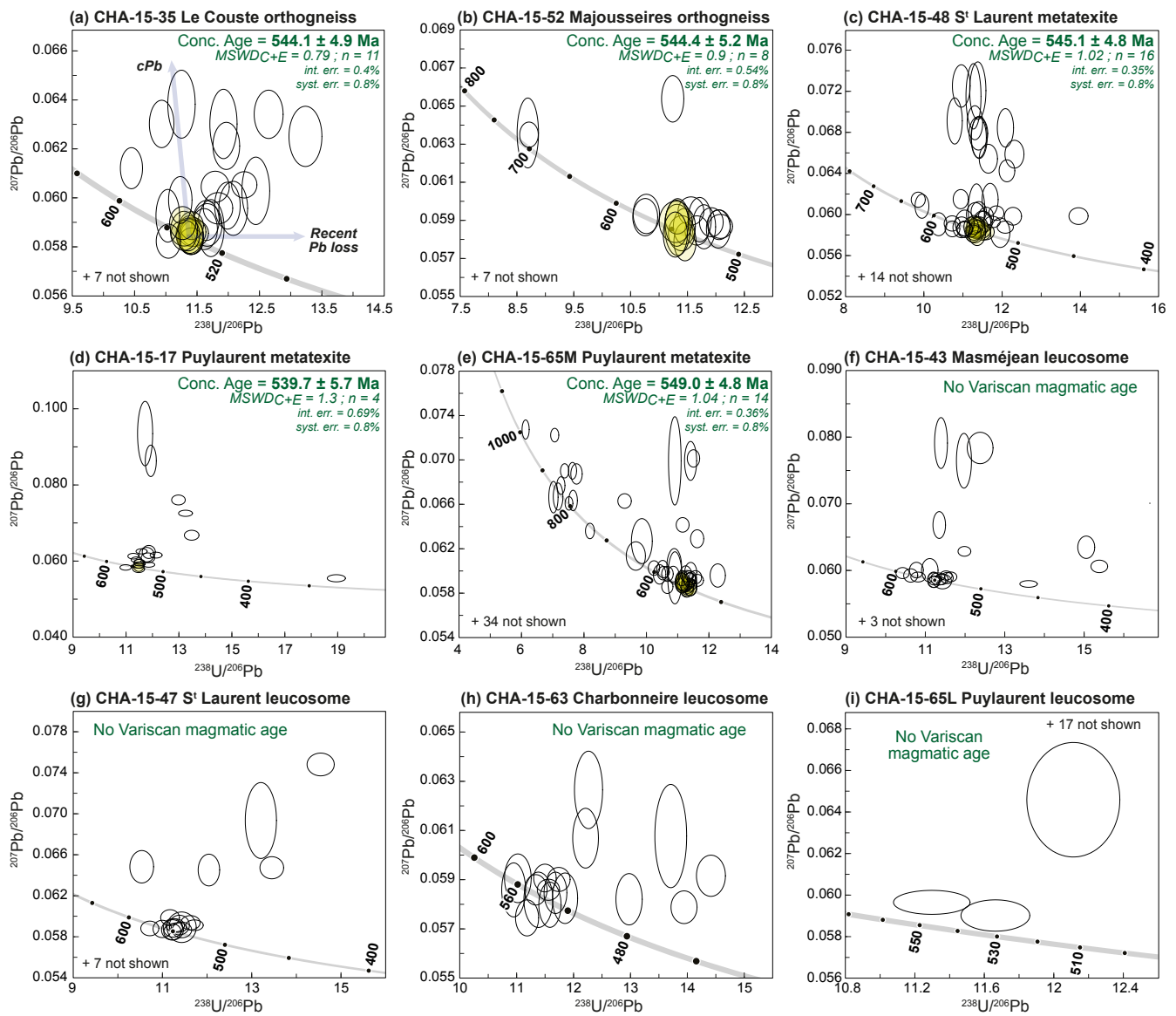


Figure 9: Tera-Wasserburg diagrams ( $^{238}\text{U}/^{206}\text{Pb}$  vs.  $^{207}\text{Pb}/^{206}\text{Pb}$ ) for zircon grains from the orthogneiss, metatexites and leucosome samples. Error ellipses and dates are displayed at  $2\sigma$  level of uncertainty. Yellow ellipses are those considered for Concordia date calculations.

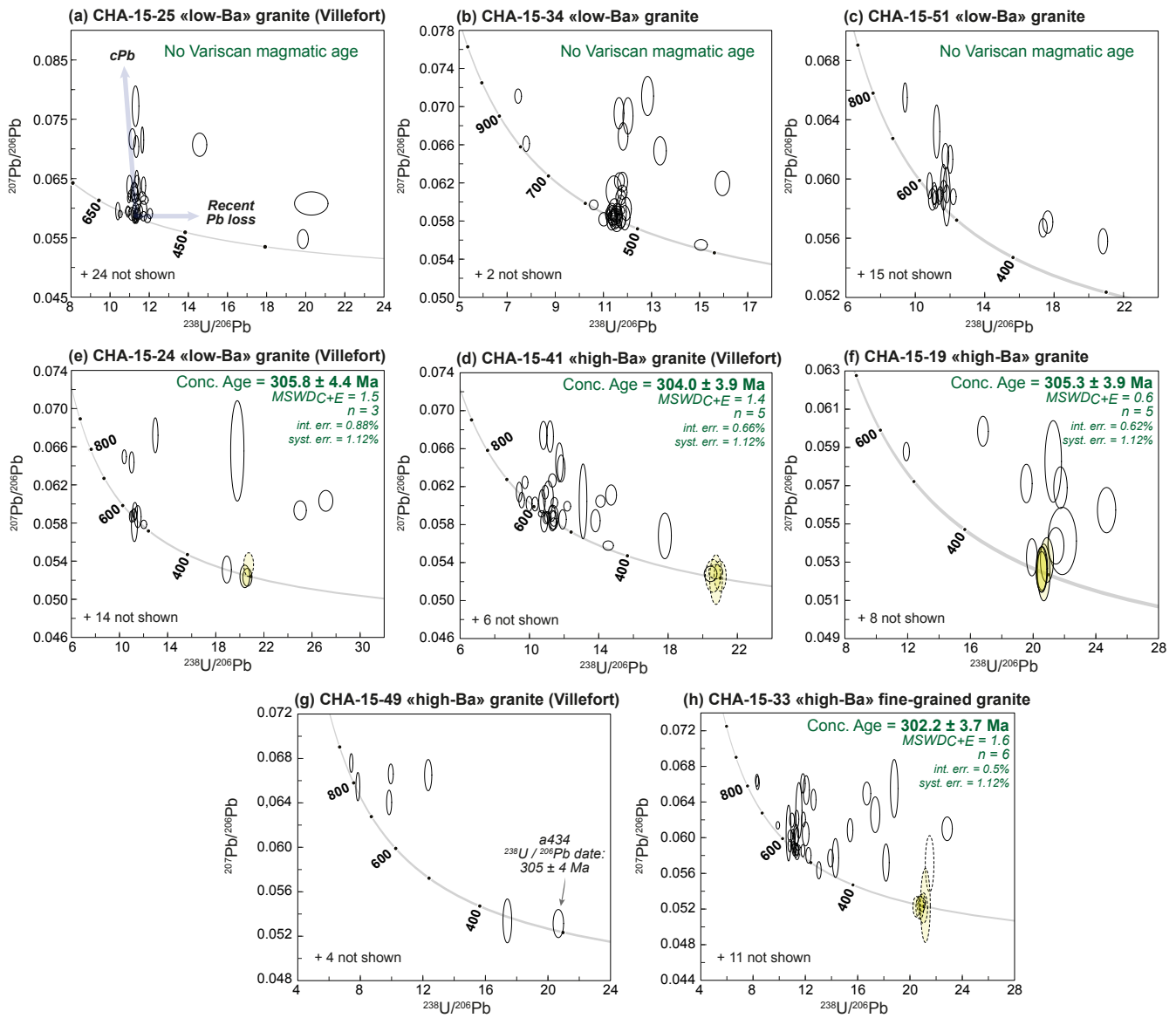


Figure 10: Tera-Wasserburg diagrams ( $^{238}\text{U}/^{206}\text{Pb}$  vs.  $^{207}\text{Pb}/^{206}\text{Pb}$ ) for zircon grains from granite samples. Error ellipses and dates are displayed at  $2\sigma$  level of uncertainty. Yellow ellipses are those considered for Concordia date calculations.

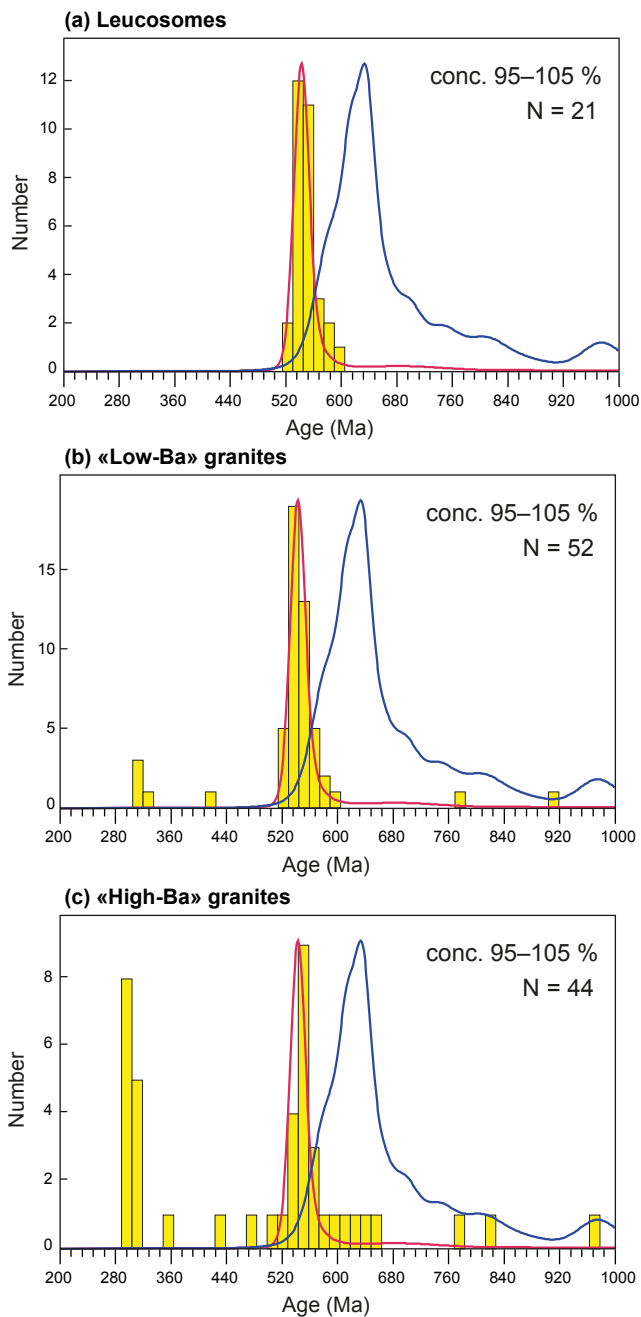


Figure 11: Histogram showing the  $^{206}\text{Pb}/^{238}\text{U}$  dates measured on zircon grains from leucosomes and granites. Bin width is 15 Ma. Available zircon  $^{206}\text{Pb}/^{238}\text{U}$  dates (concordance: 95–105%) for the Velay Orthogneiss Formation (in red) and regional metasediments (in blue, N=107 and 445, respectively) are from Chelle-Michou et al. (2017), Couzinié et al. (2019); Couzinié et al. (2017) and this study, represented as Kernel Density Estimates. The latter were calculated using the DensityPlotter program of Vermeesch (2012) with a bandwidth set at 15 Ma.

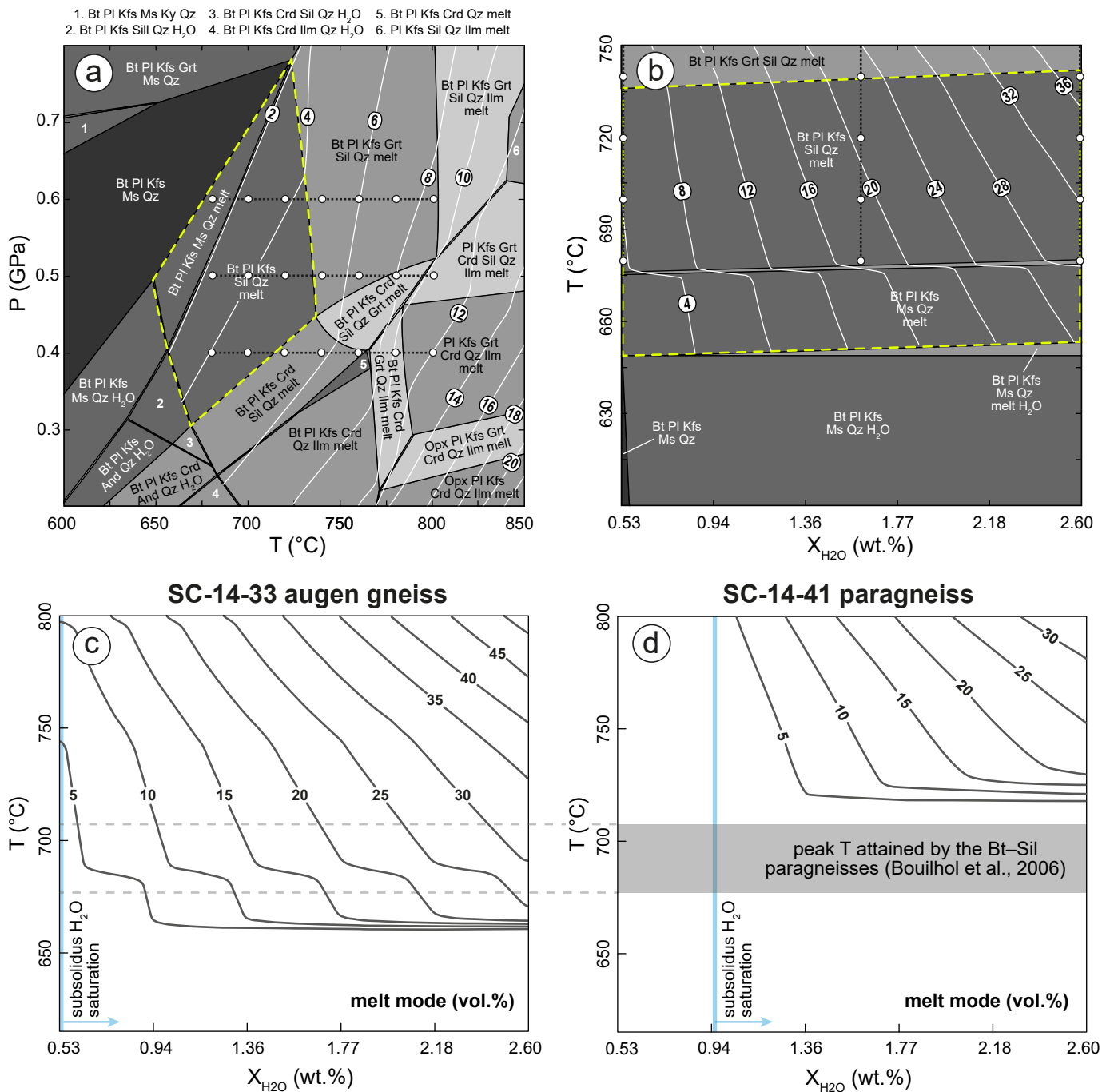


Figure 12: (a, b) P–T and T–X<sub>H2O</sub> pseudosections calculated using a representative orthogneiss composition (SC-14-33, from Couzinié et al. (2017)). White lines are melt modes (with numbers indicating melt vol.%). Initial water content of 0.53 wt.% for the P–T pseudosection was adjusted to avoid subsolidus water saturation at 0.5 GPa. Mineral abbreviations after Whitney and Evans (2009). The white dots connected by black dashed lines refer to the location in the P–T–X<sub>H2O</sub> space of the melts for which equilibrium Ba–Sr–Rb–Nb compositions have been computed. These calculations rely on the thermodynamically-constrained phase proportions and a set of partition coefficients for felsic systems compiled by Laurent et al. (2013) and listed in Supplementary Table S6. (c, d) Comparison of respective melt productivities (in vol.%) for representative augen gneiss and paragneiss samples (samples SC-14-33 and -41, respectively) at T < 800°C and variable water contents (for a pressure of 0.5 GPa). The pseudosection for SC-14-41 (whole-rock composition available Supplementary Table 1) was calculated using the same procedure and solution models as mentioned in section 3.3.

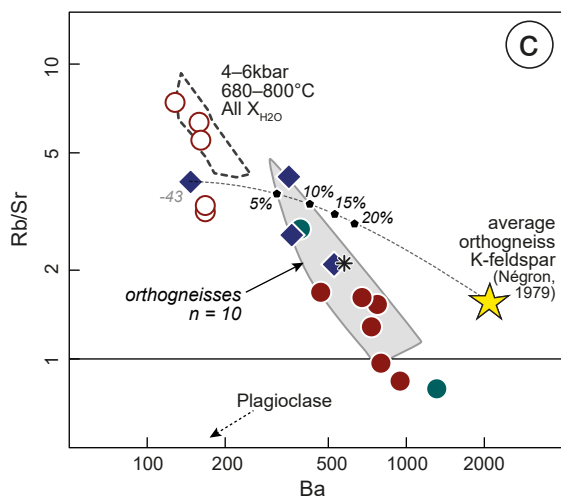
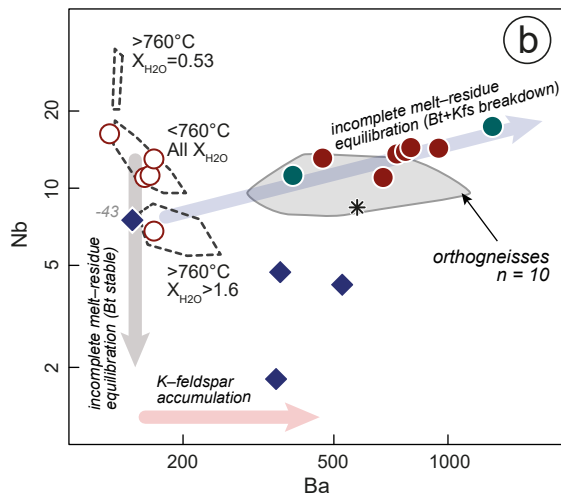
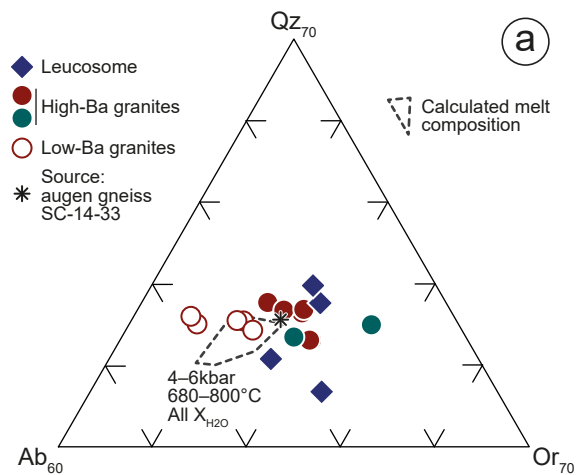


Figure 13: Petrogenesis of the Masméjean antiform leucosomes and granites. Geochemical comparison between leucosomes/granites and calculated melt compositions: (a) CIPW-normative ternary diagram; (b) Rb/Sr vs. Ba diagram; (c) Nb vs. Ba diagram. The Ba–Rb–Sr ortho composition of K-feldspar from the local augen gneisses is from Négron (1979) while that of plagioclase is estimated from Bea et al. (1994).

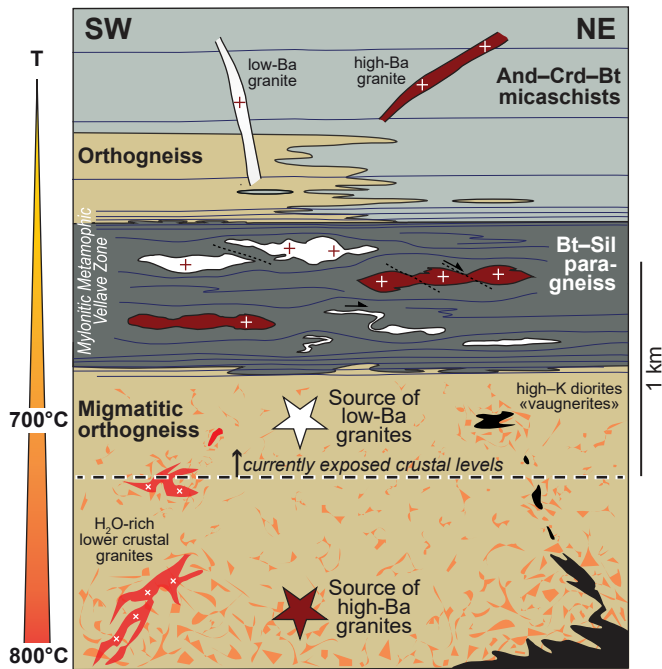


Figure 14: Sketch cross-section through the southern Velay mid-crust (c. 10–15 km depth) at c. 305 Ma, right before the onset of doming. The Mylonitic Metamorphic Vellave Zone (MMVZ) corresponds to a high-strain shear zone developed at the interface between the anatexitic and unmolten domains. Granite magmas formed at the expense of the orthogneisses were either emplaced within the MMVZ or extracted to higher crustal levels where they crop out as dykes. In the partially molten domain, water-fluxed melting possibly resulted from (i) diffusive transfer of magmatic H<sub>2</sub>O along chemical potential gradients between orthogneisses and water-rich granitic melts ( $X_{\text{H}_2\text{O}} > 8$  wt.%) generated at pressures in excess of 1 GPa (>35 km depth, considering average crustal density of 2700 kg.m<sup>-3</sup>, left part of the figure); (ii) the exsolution of magmatic water following the crystallization of high-K dioritic bodies (“vaugnerites”, right part of the figure).

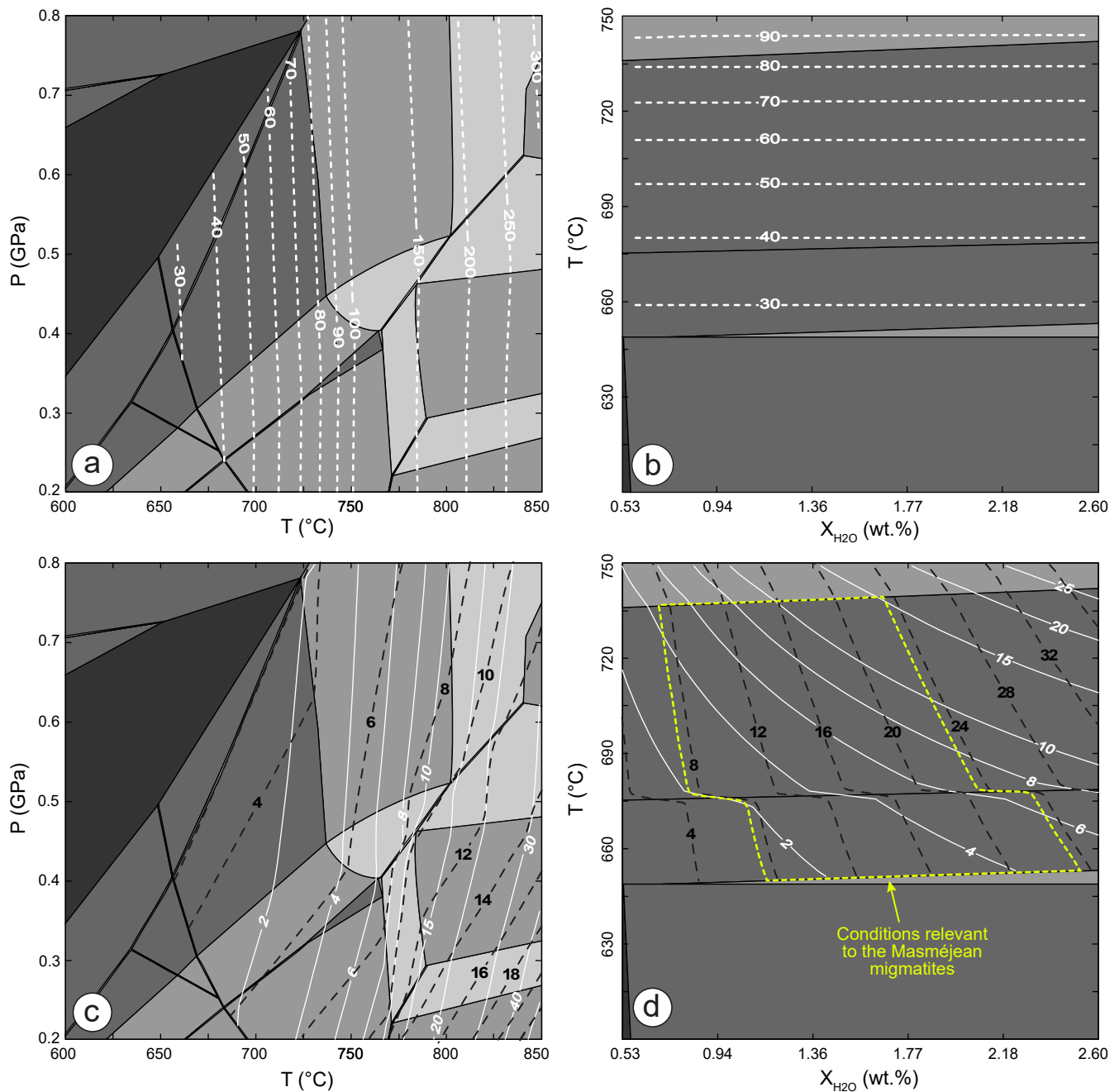


Figure 15: (a) and (b): calculated maximal Zr concentration (in ppm) in the melt phase for a fully hydrated (at 0.5 GPa) orthogneiss composition (SC-14-33) in the P–T space and along a T– $X_{H_2O}$  section set at 0.5 GPa, based on the solubility equation of Boehnke et al. (2013). The Zr concentration of the stoichiometric zircon was set at 497644 ppm and the average Zr content of the protolith at 115 ppm (average value for the local augen gneisses, data from Couzinié et al. (2017)). (c) and (d): calculated proportion (white lines, in wt.%) of the orthogneiss zircon budget to be dissolved in order to saturate the melt phase. Black dotted lines and bold numbers are melt modes in vol.%.